University of Zurich[UZH]

Master's Thesis

Cosmic Muons to calibrate Xenoscope

Swayamsiddha Joshi

Professor: Prof. Dr. Laura Baudis

Spervision: Dr. Michelle Galloway, Dr. Neil McFadden

University of Zurich

May 19th, 2022

Acknowledgements

First and foremost, I would like to express my gratitude to Prof. Dr. Laura Baudis for granting me this wonderful opportunity of working on this project. It has been a great learning experience for me. A very big and special thanks to Dr. Michelle Galloway who has given me her valuable advice and support throughout this work. For all her time and efforts, I shall always remain grateful. I would also like to thank Dr. Neil McFadden for the initial idea of this project and for guiding me through it. To all the group members especially, Yanina Biondi, Alexander Bismark, Frederic Girard, Ricardo Peres, Diego Ramirez and Dr. Christian Wittweg, thank you for your constant motivation and for always being there to help. A special thanks to Jose Javier Cuenca-Garcia for all his help with the thesis. I would also like to thank Jonathan Franchi for helping me with the detector setup.

Lastly, a big thank you to my parents, family and friends for always being there and to dadu for looking over me, always.

Contents

Introduction

For nearly 100 years now, the nature of dark matter has been a very important but unsolved question in physics. It all started in 1933, when Swiss American astronomer Fritz Zwicky measured the mass-to-light ratio of a galactic cluster, named Coma cluster. It was found that the observed ratio was larger than expected considering all the mass of the cluster to be luminous [1]. Hence, the existence of dark matter was hypothesized which would increase the mass of the cluster without increasing its luminosity. After this interesting finding, there has been plenty but only indirect evidence that proves the existence of dark matter. Over the years, many attempts have been made to explain its nature. Some explanations of the evidence were suggested using the theory of Modified Newtonian Dynamics (MOND) and Massive Compact Halo Objects (MACHOs). One of the important explanations of the evidence came from assuming the constituent of dark matter to be a fundamental particle. From the evidence found, some of the properties of the particle that makes up the dark matter could be deduced, such as, it should have a higher mass, have no electromagnetic interaction and a weak-scale interaction with baryonic matter. Looking at these properties, it could be said that the Standard Model does not provide a good dark matter candidate, so a new particle making up the dark matter was theorized. Weakly Interacting Massive Particles (WIMPs) are one such hypothetical class of particles that are considered to be dark matter.

There are different strategies to search for WIMPs: collider production, indirect search and direct search. In the direct search, the interaction where a dark matter particle scatters off a Standard Model particle resulting in an energy deposition can be measured in the detector. The energy deposited can be detected as three different signatures, depending on the detection technique used : charge,light and heat. The most sensitive detection technologies measure two out of these three signatures, DARk matter WImp search in liquid xenoN (DARWIN) will be one such detector that will look for the charge and light signatures. DARWIN will be based on a dual-phase Time Projection Chamber (TPC) with a liquid xenon (LXe) target [2]. DARWIN will use

some of the technologies at scales that have never been tested before. To test some of the technologies, a demonstrator for the DARWIN detector, named Xenoscope, was set up at the University of Zurich. One of the main goals of Xenoscope is to achieve the drifting of electrons in LXe over its 2.6-m height in the vertical direction by the application of an external electric field. The experiment proceeds in three phases, increasing the drift length of the electrons each time. The first phase includes a 50-cm purity monitor, the second will have a 1-m TPC and the final configuration will be the full 2.6-m TPC [3].

Purity of the xenon and the homogeneity of the applied electric field are two important conditions required to achieve the main goal. In the first phase of Xenoscope, the purity of LXe can be checked by measuring the lifetime of the electrons drifting inside the purity monitor. Currently, a xenon flash lamp is used to generate these electrons. Cosmic-ray muons ionize the xenon atoms and can be used as an alternative method for the generation of electrons. The motivation behind this project is to use cosmic muons as a trigger for the purity monitor. This will provide an additional z-dependent electron lifetime measurement. To detect the muon events, two scintillator detectors were placed on opposite sides of the LXe target. The detectors were used in coincidence to trigger data acquisition with the purity monitor. The muon detector set up could be placed at different positions with respect to the purity monitor for a z-dependent electron lifetime measurement. This set up could also be used to re-confirm the homogeneity of the electric field inside the purity monitor. In this work, the two muon detectors were designed, assembled and tested, before they could be used for calibration purposes in Xenoscope.

Chapter 1 includes a brief introduction about dark matter, the evidences leading up to what we know about it today, introduction to WIMPs and the different methods of dark matter search. The working principle and design of the DARWIN detector and its demonstrator, Xenoscope, is explained in chapter 2. The purity monitor, which is an important part of the motivation behind this project, is also explained in this chapter. In the next chapter, chapter 3, cosmic muons and their interaction with matter is introduced. It also includes the components and assembly of the detectors used for muon detection and their principles of working. The measurements done with the detectors are mentioned in chapter 4. This chapter also includes the analysis part of the experimental data. The performed simulation work and theoretical calculations required for the calibration purposes of Xenoscope using the muon detectors is explained in chapter 5. The work of this project is summarized in the final chapter of this thesis,

with an outlook of what can be done with the setup of this experiment in the future.

1 Dark Matter

Dark matter plays an important role in explaining the evolution and current status of the Universe. A total of 26.8% percentage of the energy and matter density of the Universe is made up of dark matter which makes the dark matter five times more abundant than baryonic matter. The current distribution of the energy and matter density of the Universe is shown in Figure 1 [4]. As of today, there has been plenty but only gravitational evidence pointing to its existence. There has been an ongoing search for the direct detection of dark matter in particle form but without any confirmation so far.

In the next few sections, we will discuss the early observational evidence for dark matter, suitable dark matter candidates and the basis of direct detection of dark matter.

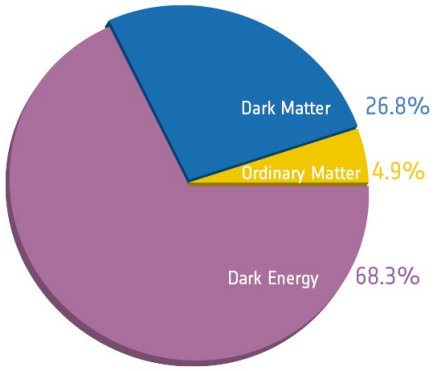

Figure 1: Recent measurements using Planck satellite shows the current distribution of constituents of the Universe, where dark matter is almost 5.4 times more than ordinary matter [4].

1.1 Evidence

1.1.1 Mass of the Coma cluster

The initial observations regarding the existence of dark matter were made by Swiss American astronomer Fritz Zwicky when the observed mass-to-light ratio of the Coma galaxy cluster came out to be larger than expected based on the luminous matter alone. The virial theorem, which relates the kinetic and potential energy of a gravitationally bound system, was used to calculate the mass, M, of the galaxy cluster:

$$\mathrm{M} = \frac{\mathrm{Rv}^2}{\mathrm{G}} \tag{1}$$

where R is the radius of the Coma cluster, v is the mean squared line-of-sight velocity obtained via redshift measurements, and G is the gravitational constant. The mass of the Coma cluster came out to be 4×10^{13} solar masses [1]. For the mass-to-light ratio, the galactic mass was compared to average galactic luminosity, which is $8.75 \times 10^{7}\mathrm{L}\odot$ where $\mathrm{L}\odot$ is the solar luminosity. The cluster contains about 1000 galaxies so the average galactic mass becomes 4×10^{10} solar masses. The mass-to-light ratio was estimated to be several order of magnitudes greater than what we would expect if all the mass of the Coma galaxies came from visible matter. As an explanation out of the problem the concept of dark matter comes into play, which would increase the galactic mass without increasing the galactic luminosity.

1.1.2 Galaxy Rotation Curves

The rotation curve of a galaxy shows the dependence of the velocity in the galactic plane to the distance from the center of the galaxy. If most of the galactic mass is concentrated at the center, as is indicated by its luminosity, the velocity of the stars would decrease with increasing distance from the center, $\mathrm{V_r} \propto \mathrm{r}^{-1}$.
In case of a spherical symmetry, the centrifugal force acting on a mass (m) at a distance R from the center of the galaxy becomes equal to the gravitational attraction:

$$\frac{\mathrm{mV_r^2}}{\mathrm{r}} = \frac{\mathrm{GM_r m}}{\mathrm{r}^2} \tag{2}$$

$$\mathrm{V_r} \propto \sqrt{\mathrm{r}^{-1}} \tag{3}$$

Contrary to what it was expected, as shown in figure 2, the observations show a flat region of velocities up to a large radii. The initial observations were made by Vera Rubin for the Andromeda galaxy which is a spiral galaxy [5]. This figure also shows the dark matter halo contribution and the disk and gas contribution needed to match the observed data. This provided further evidence for the possible existence of a large quantity of non-luminous galactic mass.

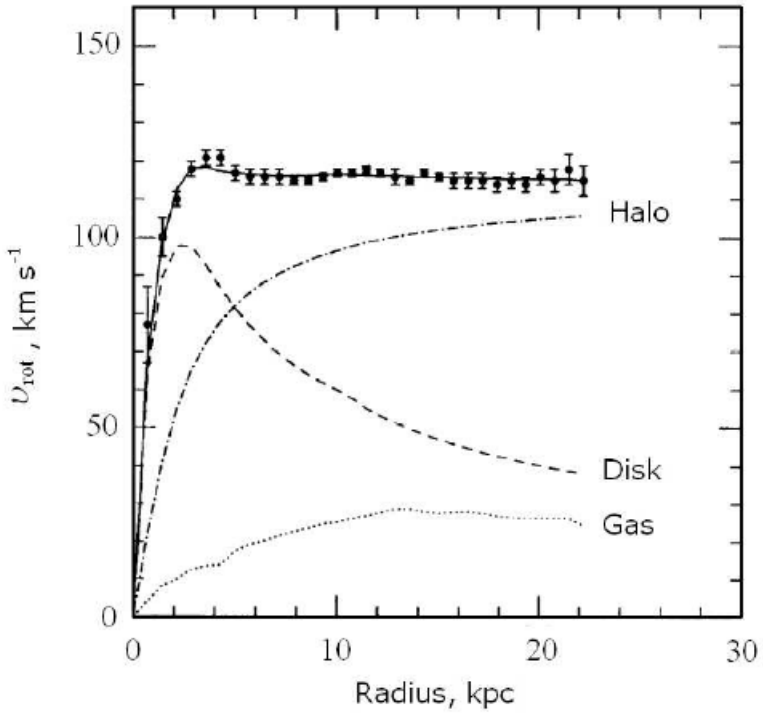

Figure 2: Galactic rotation curve shows the orbital velocity of visible stars of Andromeda galaxy as a function of the distance from the center. The observed galactic rotation curve does not fall off as $\sqrt{r^{-1}}$, which should be the case if the only constituents of the galaxy were ordinary matter [6].

1.1.3 Gravitational lensing and the Bullet Cluster

The Bullet Cluster, as shown in figure 3, was formed by the collision of two large clusters of galaxies. The two pink clumps in the image show most of the baryonic matter of the two clusters, whereas the blue areas show the total concentration of mass of the clusters that astronomers found using weak gravitational lensing. Weak gravitational lensing is a technique used to measure the masses of astronomical objects using the fact that light from distant objects is distorted by intervening matter. The

composite image shows the spatial offset of the center of the total mass from the center of the baryonic mass, which cannot be explained without the existence of dark matter.

Figure 3: Interaction of plasma and gas of the galactic clusters during their collision emits X-rays measured by the Chandra Space telescope. The stars of the resulting Bullet cluster were observed using the Hubble and Magellan telescopes, and the total matter of the cluster was measured using weak gravitational lensing. A composite image of all these observation shows the difference between the center-of-mass of total matter, shown in blue and baryonic matter of the cluster, shown in pink [7].

1.1.4 Anisotropies in the Cosmic Microwave Background

The presence of dark matter in the Universe can be measured from the Cosmic Microwave Background (CMB). The temperature of the Universe was very high at the Big Bang and has decreased continuously as the Universe expanded to the present state. Right after the Big Bang, the Universe was in a state referred to as quark soup which contains quarks and gluons in thermal equilibrium. To maintain this thermal equilibrium, the particles had to be constantly interacting with each other. As the Universe expanded, the interaction rate dropped and the particles decoupled and froze out once their interaction rate fell below the expansion rate of the Universe. Roughly 10^5 years after the Big Bang, electrons and protons started to combine to form neutral atoms. Due to this drop in electron number density, the Universe became transparent to photons; these photons are observed today as the Cosmic Microwave Background. The CMB is the last scattering surface of photons and its spectrum is very close to that of a blackbody. The anisotropies in the CMB consists of small temperature fluctuations at the level of about 1 part in 100,000 left over from early Universe, as shown in Figure 4 . The angular power spectrum of the anisotropy of

the CMB contains information about the formation of the Universe and its current contents. This angular power spectrum quantifies how much the temperature varies from point to point on the sky vs. the angular frequency. The power spectrum depends on the densities of the baryonic matter, cold dark matter and dark energy. The most precise measurements of these cosmological parameters have been performed by the Planck satellite and the density of cold dark matter (Ω_c) in the universe came out to be [8]:

$$\Omega_c h^2 = 0.120 \pm 0.001 \tag{4}$$

which implies that about 26% of the Universe is dark matter. Here, Ω_c is defined as the ratio of the cold dark matter density (ρ_{CDM}) in the present day Universe to the critical density (ρ_c). Here, $\rho_c = \frac{3H_0^2}{8\pi G}$, where H_0 is the expansion rate of the universe at present, known as Hubble's parameter and G is the gravitational parameter. h is the reduced Hubble expansion parameter defined as, $h = \frac{H_0^2}{100 \text{ km s}^{-1} \text{ Mpc}^{-1}}$.

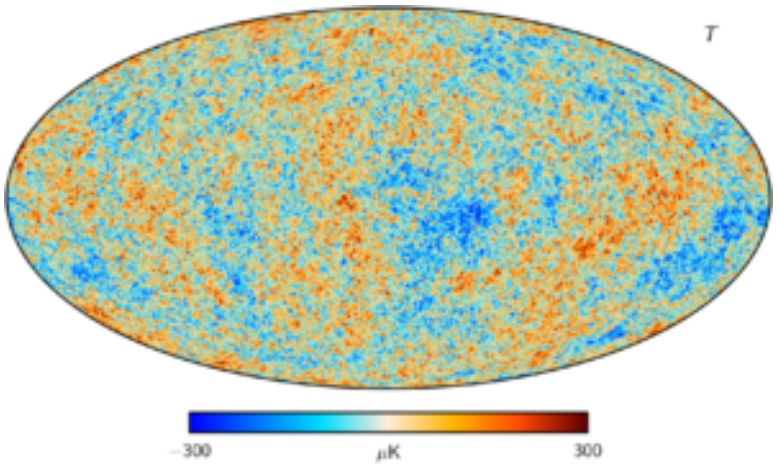

Figure 4: Map of the temperature fluctuations in the Cosmic Microwave Background measured by the Planck satellite [9]. Measurements of this temperature fluctuations of the CMB plotted as a function of angular frequency give the dark matter density currently present in the Universe.

1.2 Dark Matter Candidate: WIMP

From the observational evidence a few characteristics of a suitable dark matter candidate can be concluded: it should be neutral (no electromagnetic interaction), it should be stable and cold (non-relativistic). The Standard Model of particle physics does not contain a single suitable dark matter candidate; therefore it is assumed that

dark matter must be made of new particles that have not been detected yet. Weakly Interacting Massive Particles (WIMPs) are one such new hypothetical class of particles that are considered to be the constituents of dark matter. WIMPs are expected to have masses in the range $m \sim 1 - 10^5$ GeV/c^2 [10] with a cross-section of interaction between WIMPs and nucleons being $10^{-41} - 10^{-51}$cm^2 [10]. Many WIMP candidates are predicted to have been produced thermally in the early Universe after the Big Bang, similar to baryonic particles. As explained in section 1.1.4 , moments after the Big Bang, the Universe is in a dense and hot state, and all particles are in thermal equilibrium. When the temperature of the Universe is higher than the rest mass of a certain particle, the photon energy is high enough and can create the particle and its antiparticle. The interaction rate of the dark matter particles with each other is greater than the expansion rate of the Universe. As the Universe expands and cools down, the number density of dark matter particles begin to decrease as they begin to annihilate. However, it doesn't drop to zero because as the Universe expands the dark matter particles cannot find each other to annihilate. When the weak interaction rate of the dark matter particles falls below the expansion rate of the Universe, the number of dark matter particles freezes out.

The interaction rate can be written as, $n_{DM}\sigma_{DM}v_{DM}$ where n_{DM} is the number density of the dark matter particle, $< \sigma_{DM}v_{DM} >$ is the thermally averaged cross-section of interaction of the dark matter (DM) particles with each other. By equating the DM-DM interaction rate with the expansion rate of the Universe, a relation between the dark matter abundance and the interaction cross-section can be found. Using the weak-scale interaction cross-section in this relation gives the correct value of relic dark matter abundance. This is called the WIMP miracle: Weak scale particles make excellent dark matter candidates.

1.3 Detection of WIMP dark matter

There are three different ways to search for WIMPs: looking for WIMPs produced at collider experiments by interaction of Standard Model particles, indirect search, where the interacting particles are WIMPs that annihilate and produce Standard Model particles, direct search that looks for WIMPs that interact with the target nuclei.
Indirect detection experiments look for detection of dark matter via decay or annihilation into Standard Model (SM) Particles. Direct detection experiments are designed to observe SM-DM scattering, and collider experiments aim to detect dark matter

particles produced in high-energy particle collisions. The three different searches and their corresponding interaction is shown in Figure 5. In the following sections these three processes will be discussed in a little more detail.

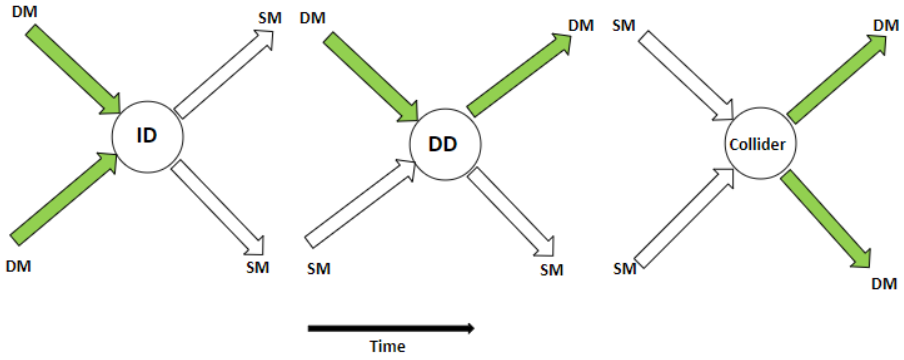

Figure 5: Illustration of different dark matter detection techniques with time flowing from left to right. Here, ID refers to Indirect detection, DD refers to direct detection, SM and DM refer to Standard Model particle and dark matter particle respectively.

1.3.1 Collider Production of WIMP

The collider searches use the fact that dark matter particles can be produced from colliding Standard Model particles through SM SM $\rightarrow$ DM DM interaction. DM cannot be detected, hence making the DM particle undetectable but such events are accompanied by production of one or more SM particles. For example, in the Large Hadron Collider (LHC) protons are the colliding particles. In LHC, the presence of a dark matter particle would be detected by observing events with missing transverse momentum and energy as the missing energy can be associated with the dark matter particle.

1.3.2 Indirect Detection of WIMP

The dark matter particles can annihilate through DM DM $\longrightarrow$ SM SM and give pairs of Standard Model particles and their antiparticles like electrons, positrons, and gamma rays, which can be observed in various types of detectors [11]. They search for signals of WIMP annihilation from areas with expected higher dark matter concentration such as Dwarf spheroidal galaxies.

1.3.3 Direct Detection of WIMP

Dark matter can scatter off normal matter through DM SM $\rightarrow$ DM SM interactions. This could be observed in very sensitive detectors that minimize the radioactive background. Searches in the GeV-TeV mass range of WIMPs look for nuclear interaction. This is because higher mass WIMPs will preferentially not interact with atomic electrons but will instead elastically scatter off the atomic nucleus. The momentum transfer gives rise to a nuclear recoil which might be detectable. The recoiling nuclei can deposit energy in the medium of the detector via three different processes: scintillation from de-excitation of the molecules, atomic ionization and heat production. The nuclear recoil energy is typically in keV range. The expected rate of WIMPs scattering off a target nucleus of mass m_N is given by [12]:

$$\frac{dR}{dE_R} = \frac{\rho_0}{m_X m_N} \int vf(v) \frac{d\sigma}{dE_R} d^3v \tag{5}$$

The above equation gives the interaction rate per recoil energy unit per detector mass, where E_R is the energy of the nuclear recoil, v is the WIMP velocity relative to the target, f(v) is the WIMP velocity distribution, σ is the total elastic scattering cross-section of WIMPs on ordinary matter, ρ_0 is the local WIMP density and m_X is the mass of the WIMP. As seen in equation 5, the interaction rate depends on a few astrophysical parameters like ρ_0 and v. So, for the direct detection experiments, the standard halo model is taken into account with $\rho_0 = 0.3$ GeV/cm^3 [13] and $v_0 = 220$ km/s [14].

As shown in equation 5, the interaction rate of the WIMPs depends on the elastic scattering cross-section which depends on how WIMPs couple to the target nucleus. This interaction can either be spin dependent or spin independent. The total cross-section is the sum of the spin independent and the spin dependent interaction cross-sections. Nucleons being fermions, follow the Pauli's exclusion principle and have alternating spin in the nucleus. For spin dependent interactions, the contributions from different nucleons cancel out, making the total cross-section zero for an even nucleon numbered nucleus. For a nucleus with odd number of total nucleons, the total spin dependent cross-section becomes equal to the cross-section of interaction of the WIMP with one nucleon. Figure 6 shows the interaction rate of WIMPs for various target materials.

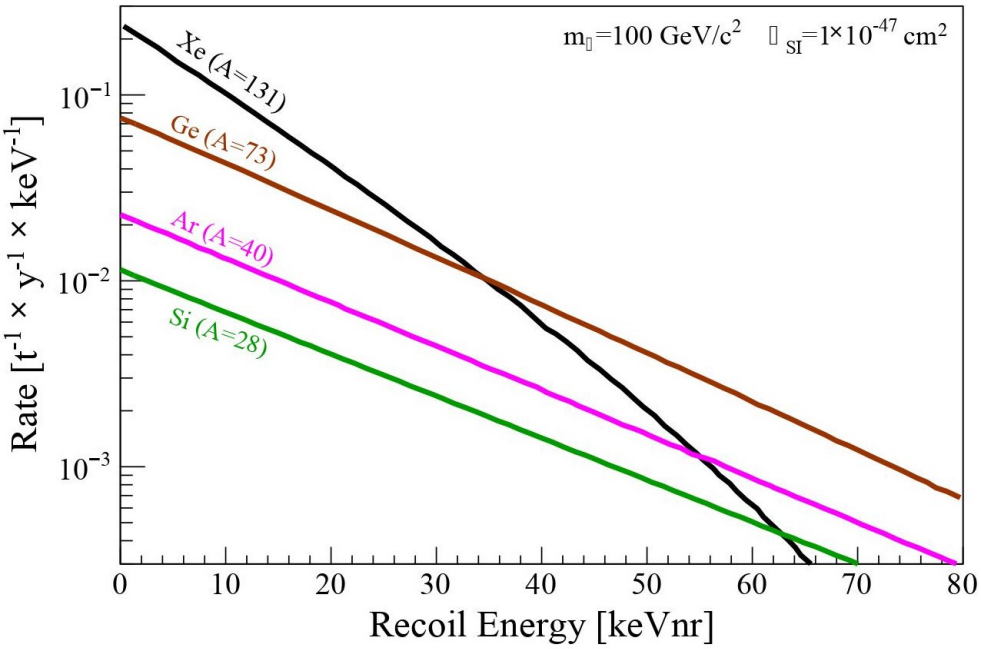

Figure 6: Direct interaction rate of a WIMP with mass 100 GeV/c^2 in different target materials as a function of the energy deposited by the nuclear recoil. Detectors with high atomic mass number target material are optimal for direct detection technique, as these conditions give higher interaction rate for low recoil energies [12].

In case of a spin independent interaction, the WIMPs interact with all the nucleons in the same way, making the spin independent cross-section proportional to the total number of nucleons. The spin independent interaction cross-section scales as A^2 where A is the atomic mass number of the target material, making the total cross-section and in turn the interaction rate proportional to A^2. This makes heavier target materials preferable for direct dark matter searches. One of the reasons for xenon being an excellent target material is its high mass number.

Direct detection experiments all over the world are trying to detect the small and rare event induced by the DM particle. An overview of the spin independent WIMP-nucleon scattering cross-section limits for the current direct detection experiments is shown in figure 7. LXe TPCs provide the strongest constraints above WIMP mass of $\sim$ 3 GeV/c^2.

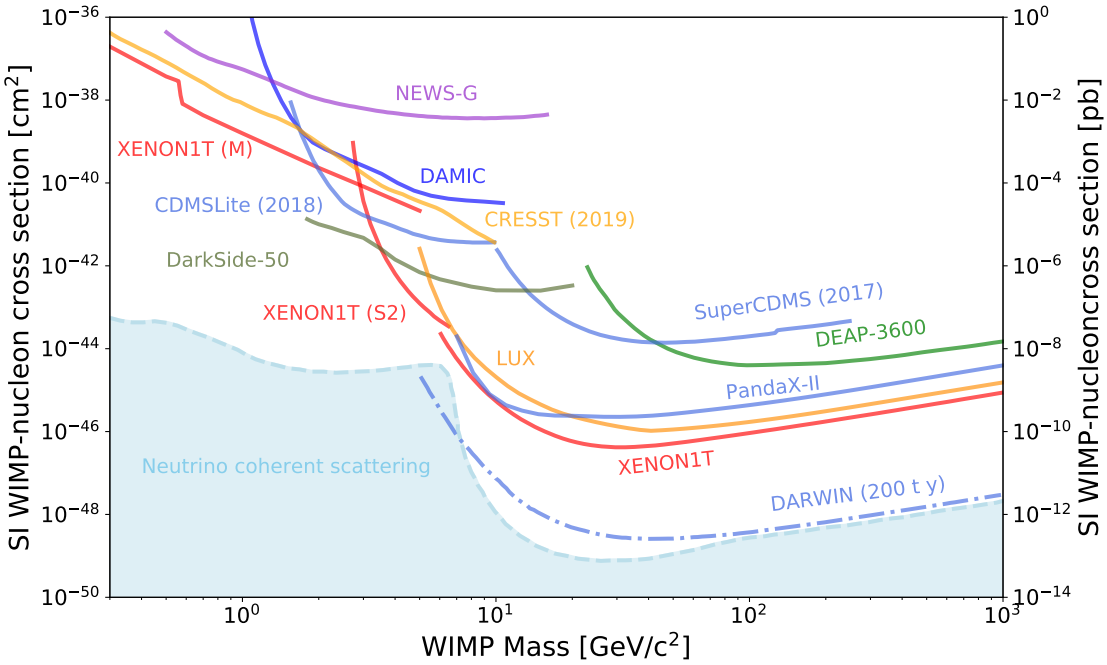

Figure 7: Current status of searches for WIMP-nucleon spin independent elastic scattering [15]. DARWIN, a future LXe TPC detector is expected to provide strongest constraints above WIMP mass of ~ 3 GeV/c^2.

2 DARWIN and Xenoscope

As discussed in Section 1.3, there are three possible WIMP signatures that can be looked for using direct detection techniques:
a) Light: excitation of the recoiling nuclei which emits scintillation light while de-excitation
b) Charge: Ionization of the atoms which provide detectable free charges
c) Phonons: Heat production
There are a wide range of detectors designed to measure one or in some cases, two of these signatures. Cryogenic bolometers operating at mK temperature are used to detect phonons. Phonon excitations are produced as a result of the conversion of kinetic energy of the scattering particle to lattice vibrations in crystals. Similarly, germanium detectors and liquid noble gas detectors are used to look for charge and light signatures respectively. Detectors that record a combination of the two signals have an upper hand because the relative size of the two signals can be used to eliminate background such as electron recoil. For example, scintillating bolometers are designed for phonon and light detection, germanium or silicon crystals to measure phonon and charge, and double phase (gas-liquid) noble-gas detectors for charge and light read-out. In this section, one such double phase noble gas detector, DARWIN (dark matter WImp search with liquid xenon) will be discussed in detail.

2.1 The DARWIN experiment

Detectors designed for the detection of WIMPs must offer a low energy threshold such that the smallest recoil energy can be detected, a very low background contamination, a large active mass and long observation time to increase the interaction probability. DARWIN will be an experiment that offers a 50 ton total and 40 ton active LXe target with high scintillation and ionization yields. Alongside its search for WIMPs, DARWIN's multiton liquid xenon TPC will also search for solar pp-neutrinos with high statistics [16],[17], coherent neutrino nucleus interactions, solar axions and galactic

axion-like particles (ALPs), as well as the neutrinoless double beta decay of the ^{136}Xe isotope [16],[18].

2.1.1 Working Principle

As mentioned earlier, DARWIN will operate a multiton LXe TPC. The energy transferred by the particle interacting with xenon is split between ionization, where electrons and ions are produced and excitation where an exciton is produced. The exciton interacts with its neighbouring xenon atoms and produce excited molecular states, excimers, which further dissociates into xenon atoms emitting a scintillation light which is in the VUV range [19]:

$$\mathrm{Xe}^* + \mathrm{Xe} + \mathrm{Xe} \longrightarrow \mathrm{Xe}_2^* + \mathrm{Xe}$$
$$\mathrm{Xe}_2^* \longrightarrow 2\mathrm{Xe} + \mathrm{h}\nu$$

The electron ion pair produced through ionization can either recombine to form excited molecular states or the electrons can escape the interaction site. The process of formation of excimers by recombination of the electron ion pair is shown below:

$$\mathrm{Xe}^+ + \mathrm{Xe} \longrightarrow \mathrm{Xe}_2^+$$
$$\mathrm{Xe}_2^+ + \mathrm{e}- \longrightarrow \mathrm{Xe}^{**} + \mathrm{Xe}$$
$$\mathrm{Xe}^{**} \longrightarrow \mathrm{Xe}^* + \mathrm{heat}$$
$$\mathrm{Xe}^* + \mathrm{Xe} + \mathrm{Xe} \longrightarrow \mathrm{Xe}_2^* + \mathrm{Xe}$$
$$\mathrm{Xe}_2^* \longrightarrow 2\mathrm{Xe} + \mathrm{h}\nu$$

The detection principle for DARWIN will be a dual phase TPC, as shown in figure 8, that measures both, the scintillation signal (S1) and the ionization signal (S2) from the particle interaction. The TPC consists of LXe target with a layer of the gaseous xenon on top. Once the particle interacts with the LXe target, the scintillation signal S1 is detected by the array of photosensors above and below the target. The ionization electrons will be drifted by a homogeneous electric field to the liquid-gas boundary which then will be extracted to the gaseous phase by a strong extraction field. The acceleration of the electrons in the strong electric field region will produce a electroluminescence signal, S2, which is proportional to the number of ionized electrons.

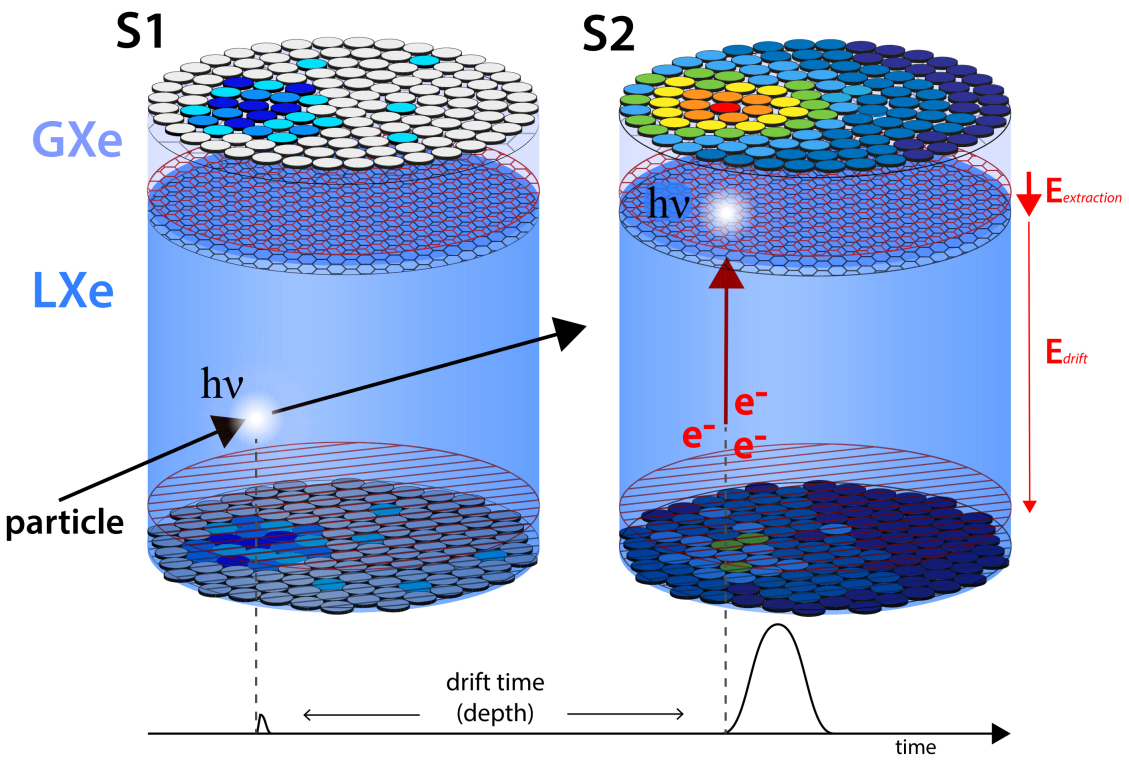

Figure 8: Schematic view of the working principle of a dual phase TPC. The scintillation signal (S1) is observed in the photosensor arrays. The electrons produced via ionization of the xenon atoms are drifted to the liquid-gas interface by the drift field, E_{drift} where they are extracted to the gas phase by the extraction field, $E_{extraction}$, producing the second signal (S2) [20].

The 3D position resolution of the interaction will be obtained via the two signals, the Z position of the interaction will be deduced by the time difference between the two signals, whereas the X-Y position will be reconstructed using the distribution of light of the S2 signal in the top PMT array. To differentiate between nuclear recoils and electronic recoils and eliminate electronic recoil background, the ratio of the two signals is used since

$$\left(\frac{\mathbf{S2}}{\mathbf{S1}}\right)_{\mathbf{ER}} > \left(\frac{\mathbf{S2}}{\mathbf{S1}}\right)_{\mathbf{NR}} \tag{6}$$

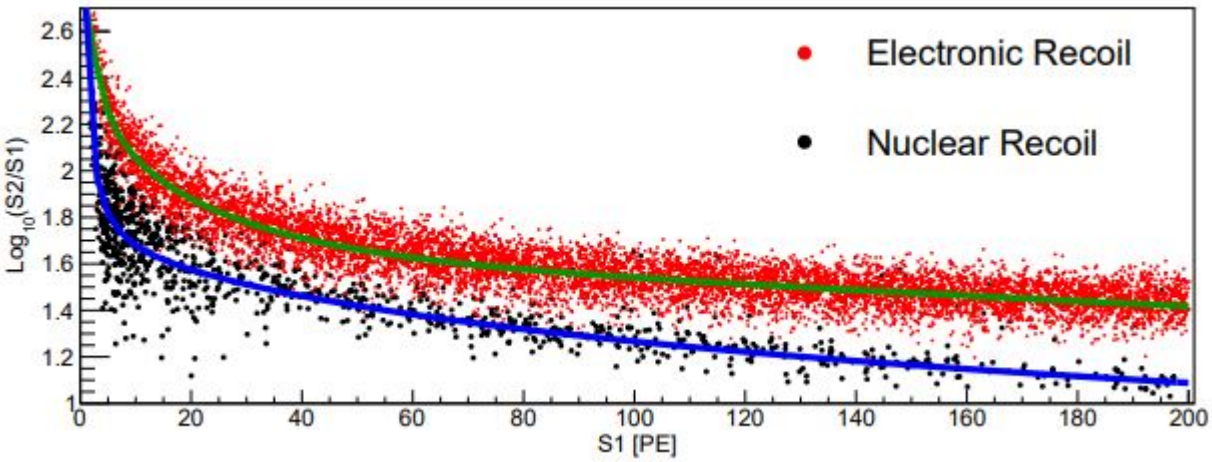

Figure 9: Ratio of S2 to S1 is different for electronic and nuclear recoil making the exclusion of electronic recoil events (background) from the nuclear recoil events (data) easier. This plot is done using the external and internal calibration sources by the XENON collaboration.

Due to their low scattering cross section, WIMPs are expected to undergo single scattering, a low background can therefore be further achieved by rejecting multiple scattering interactions.

2.1.2 Design of the TPC

The initial design of the DARWIN TPC detector will have a 2.6 m diameter and 2.6 m height which will contain the xenon mass. Arrays of photosensors will be installed above and below the liquid xenon target to detect the scintillation signals, as shown in figure 10. To drift the electrons across the TPC, a drift field of 0.5 kV/cm will be required which will be achieved by biasing the cathode at the bottom of the TPC with voltages on the order of -100 kV or above [2]. Polytetrafluroethylene (PTFE) reflectors and copper field shaping rings will be used to achieve a homogeneous drift field. The detector will have a double walled titanium cryostat surrounded by a water cherenkov shield to reduce the muon and neutron background and an inner shield with Gd-doped water to reduce the background of neutrons coming from the detector material (radiogenic neutrons). The primary shielding from cosmic rays is achieved by locating the detector deep underground. The structure will be suspended from a support frame which allow for the leveling of the TPC with $\sim$ 100 micrometers precision once the outer shields and the detector are filled with liquids.

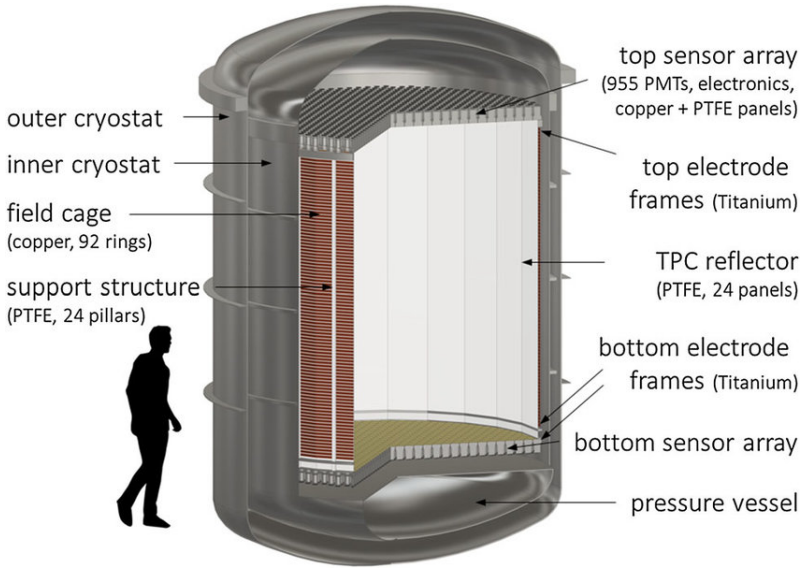

Figure 10: Time Projection Chamber of the DARWIN detector, which will have a 40-ton active LXe target. It also shows the top and bottom photosensor arrays along with the top and bottom electrodes [21].

To test some of the challenging technologies principles to be used in DARWIN, such as, the application of high voltage along its 2.6 m length, design of the purification system to improve light collection and charge yield, a full scale demonstrator, named Xenoscope in the vertical direction is built at the University of Zurich. The goals, design and working of Xenoscope will be discussed in the next section in more details.

2.2 Xenoscope

The main goal of the demonstrator is to measure the electron drift across its height of 2.6 m. This would be the largest ever attained electron drift length in liquid xenon. The two crucial conditions to acquire the goal of measuring electrons drifting over 2.6 m are:

1. High purity of LXe.

2. An adequate and homogeneous drift field.

The main requirement for any LXe TPC is that the electrons should travel undisturbed from the point of interaction in the liquid to the detection region. The impurities dissolved in LXe can absorb the electrons that are drifted by the electric field, hence decreasing the number of electrons that reach the gas phase. Therefore, the presence

of impurities in LXe must be reduced to a very low level. The purity of LXe can be maintained by continuous re-circulation of xenon through a purification system. As mentioned above, the number of electrons reaching the gas phase is also proportional to the strength and uniformity of the drift field applied. In Xenoscope, a drift field of 200 V/cm is to be achieved. This will give a drift velocity of $\sim 1.5\,\mathrm{mm}/\mu\mathrm{s}$ [22]. Hence the time taken by electrons to drift the full length of 2.6 m in order to reach the gas phase will be $\sim$ 1.75 ms. Achieving drift fields of $\sim$ 200 V/cm in a TPC with a height of 2.6 m requires a high voltage of $\sim$ 50 kV to the cathode of the detector [3]. The measurement to show electron drift of over 2.6 m will proceed in three phases in the Xenoscope, as shown in figure 11.

In the first phase, purity monitor is used that measures electron drift over 525 mm in LXe . In this phase, the flash of a xenon lamp will act as the trigger.

The second phase of Xenoscope will consist of a 1 m tall dual phase TPC with liquid level control and an extraction field that will be used to transit electrons from liquid xenon to gas xenon, generating an electroluminescence signal in turn.

In the final phase, the 2.6 m dual-phase TPC will be implemented with the cathode voltage at $\sim$50 kV to get a high enough electric field so that the electrons can be drifted through the entire length of 2.6 m.

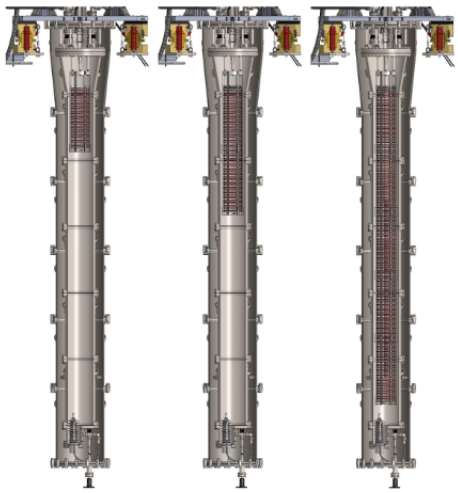

Figure 11: The three phases of Xenoscope where the first phase includes a 50-cm purity monitor (left) , the second phase will have a 1-m TPC (center) and the final phase will include the full 2.6-m configuration (right) [3].

2.2.1 Design

The TPC of the demonstrator is of the height 2.6 m which will be filled with approximately 315 kg of LXe. The TPC is placed inside a double walled cylindrical stainless steel cryostat of 312 cm height and 24.8 cm diameter. An inner frame built using aluminium profiles supports the cryostat. For the operation of the dual phase TPC, a gas handling system is used to fill gas xenon in the cryostat from the storage systems. Heat exchangers are used for the re-circulation of GXe at high speed. The purity of GXe is also maintained using the gas handling system. Liquid xenon is required for the operation of the dual phase TPC, so a cooling tower is used to liquefy the gas xenon. For the recuperation of LXe, especially in cases of emergency, a cryogenic pressure vessel, called BoX [3], is used. LXe is drained through the bottom of the cryostat directly into BoX. For GXe, an array of ten 40 litres cylindrical aluminium bottles is connected to the gas handling system, allowing to store a maximum of 470 kg of xenon [3]. Figure 12 shows all the parts of Xenoscope explained above.

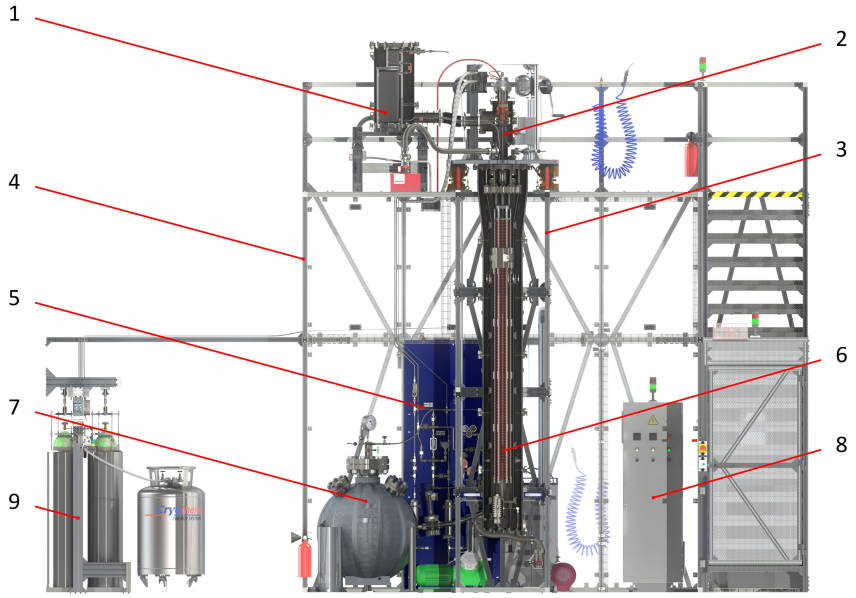

Figure 12: Schematic view of the Xenoscope facility with the 2.6-m TPC installed in the cryostat. In the figure (1) heat exchanger (2) cooling tower (3) inner frame (4) outer frame (5) purification gas panel (6) TPC in the cryostat (7) high-pressure storage vessel of liquid recovery system (8) power distribution cabinet (9) gas recovery and storage system. [3]

2.2.2 Purity Monitor

As the name suggests, a purity monitor is used to measure the purity of LXe which plays a very important role in achieving our desired goals for Xenoscope. The purity of LXe must be preserved at all times during the detector operation in order to ensure a stable performance. LXe tends to accumulate impurities $\sim$ ppm level of O_2, N_2, H_2O, as well as organic molecules. To drift the electrons along the whole length of 2.6 m, an O_2 concentration less than 1 ppb [23] is required. In Xenoscope, the purity of GXe is obtained by purification through a hot metal getter that traps electronegative impurities. For LXe, the electron survival probability (electron lifetime) can act as an indicator of its impurity concentration. The electrons drifted in LXe are absorbed by the electronegative impurities present. The attachment of the electrons to the electronegative molecules diluted in the liquid depends on the two parameters: attachment rate and the concentration of the impurities. If a number of $N_e(0)$ electrons are produced in LXe at time t=0, we expect to find a reduced number of electrons at time t, according to

$$N_e(t) = N_e(0)e^{-t/\tau} \tag{7}$$

where τ is the electron lifetime and is associated with the impurity parameters by

$$\tau = \frac{1}{K_s N_s} \tag{8}$$

where K_s is the attachment rate which is a function of the applied electric field and N_s is the number of impurities.

Working Principle of the purity monitor

The working principle of a purity monitor is based on generating electrons from a cathode and drifting them towards an anode. For the purity monitor in Xenoscope, UV light with wavelength, λ = 100-400 nm, from a xenon lamp is used to flash the photocathode, as shown in figure 13, which in turn generates electrons via photoelectric effect. By the application of an electric field, the electron bunch move towards the anode along the electric field lines where it crosses a transparent grid, producing a charge on the cathode. The drift velocity of the electrons is related to the electric field as shown in figure 14. Some of the electrons arrive at the anode by crossing another transparent grid, again producing a charge on the anode. There are three electric field regions in the purity monitor, first one between the cathode and cathode grid, second

between cathode grid and anode grid and third between the anode grid and anode. The purpose of the grids is to shield the cathode and anode from the electrons moving in the drift region between the anode grid and the cathode grid. During the drift time, attachment to the impurities may take place, reducing the amount of electron charge collected by the anode compared to cathode. The comparison of both the readings can provide an estimation of the electron lifetime, which in turn is related to the impurities in LXe.

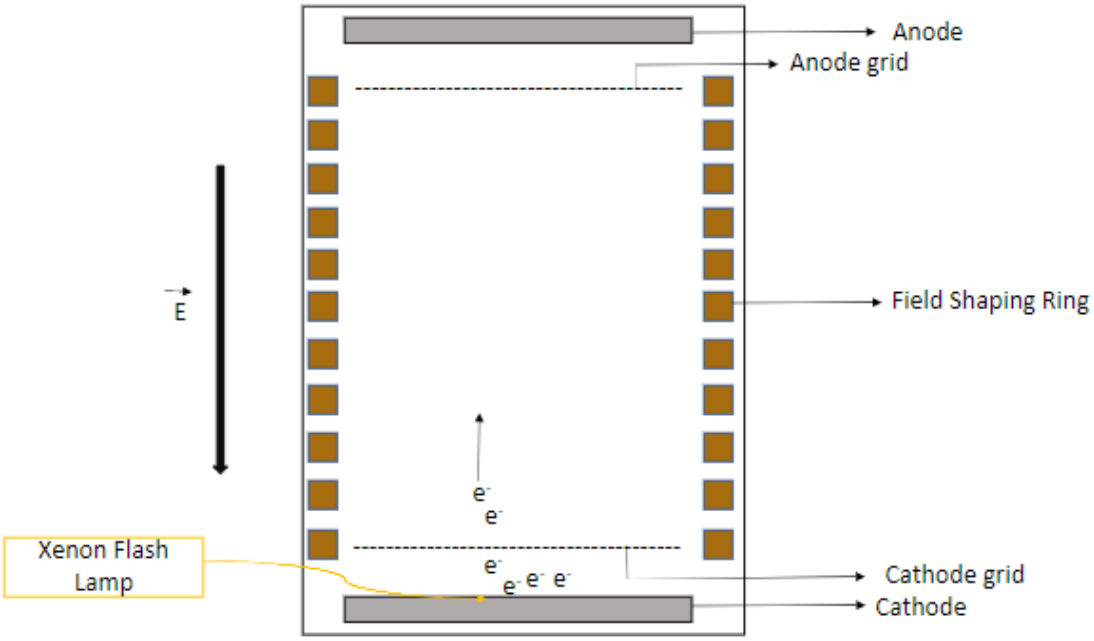

Figure 13: Sketch of the working principle of the purity monitor. Currently, a xenon lamp is used to flash the photocathode which results in production of electrons via the photoelectric effect. These electrons are drifted by the homogeneous electric field provided using the copper field shaping rings and electrodes, which are then collected at the anode.

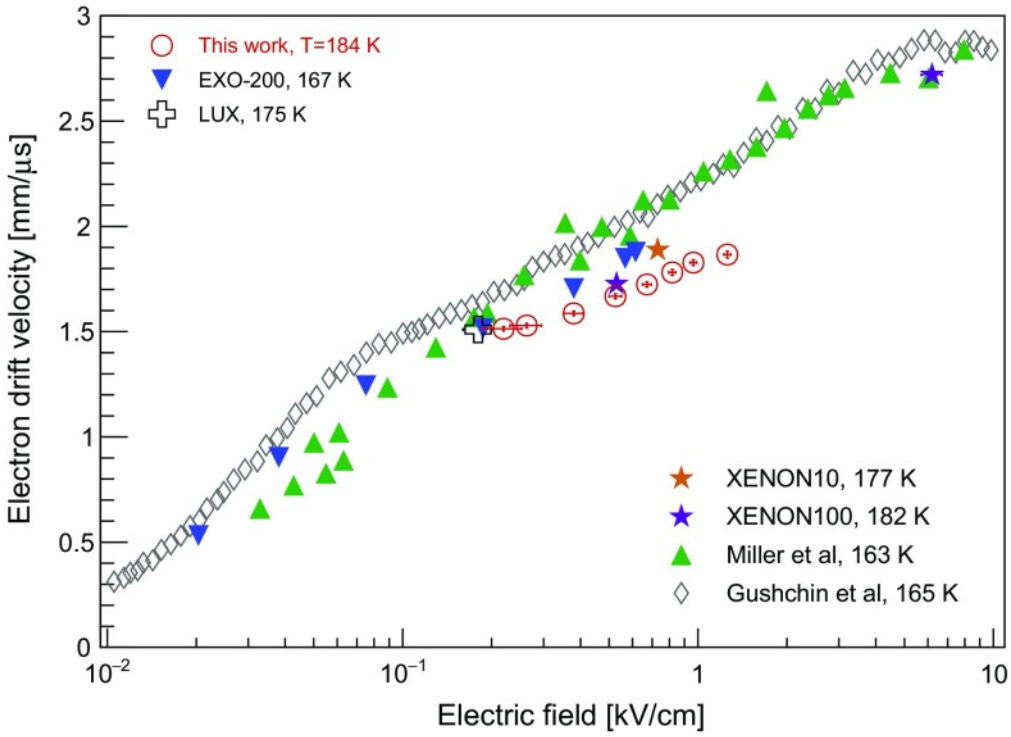

Figure 14: Variation of the drift velocity of electrons with the applied electric field as measured in different experiments. At an electric field of 200 V/cm applied in Xenoscope, the drift velocity of electrons is expected to be $\sim$ 1.5 mm/μs [24]

Mechanics and Electrical connection

The purity monitor designed for the Xenoscope consists of four parallel electrodes, the cathode, cathode grid, anode grid and anode. An optical fiber pointing at the center of the photocathode is used to flash it by a xenon flash lamp. As a result, photoelectrons produced by photoelectric effect drift in the first drift region, from the photocathode to the cathode grid and a signal is induced in the photocathode. The cathode grid is 17 mm above the photocathode. The second drift region is between the cathode and anode grids where the electrons are drifted by the applied electric field through the 525 mm length. the voltage is applied using a 10kV SHV feedthrough. When the electrons are in this region, the signal is at its maximum. The third and last drift region is between the anode grid and anode. The anode grid is placed 10 mm below the anode. A second signal is induced in the anode as the electrons drift in the third region towards the anode where the electrons are collected. The ratio between the two signals is proportional to the electron lifetime. The design of the purity monitor along

with the placement of the electrodes is shown in the figure 15.

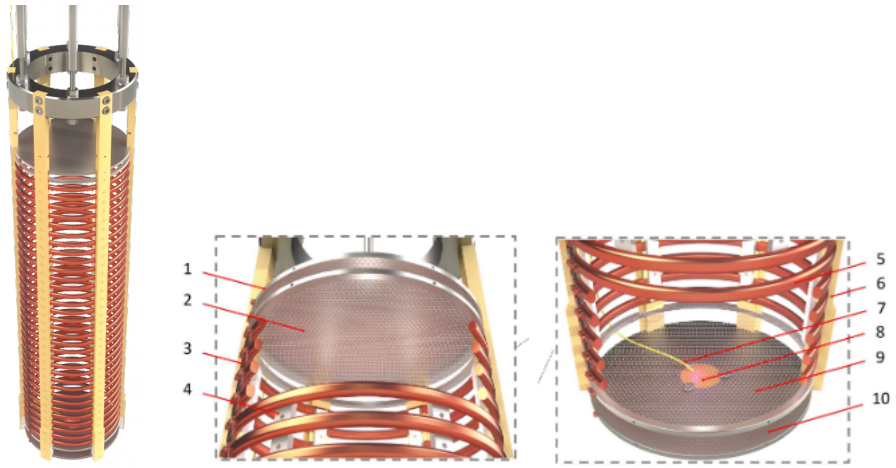

Figure 15: Purity monitor design for Xenoscope. (1) anode,(2) anode grid,(9) cathode grid,(10) the photocathode, (7) optical fiber used to flash xenon lamp, (5) copper field shaping rings,(6) polyamide-imide pillars, (4) locking blocks [3].

The field cage consists of various sections of 525 mm. These sections can be connected together to form the 1 m and 2.6 m tall drift regions for the second and third phase of Xenoscope. The field cage is made up of oxygen-free high conductivity copper rings and has an inner diameter of 15 cm. These copper rings are joined by interlocking Polytetrafluoroethylene (PTFE) pieces fixed to the inner side of the field cage. As shown in figure 15, 6 pillars made of polymide-imide are used to stack the copper rings and give it the required height. These are selected due to their good mechanical, electrical and low out-gassing properties. The pillars are connected to a stainless steel ring which is suspended under the top flange by six stainless steel rods. The High Voltage in the purity monitor phase is supplied by a NIM power supply through a 10kV CeramTec SHV feedthrough [3]. For the electronic circuit, the readings are collected from the anode and cathode. The readings from the anode and cathode are connected to HV filters and a preamplifier with positive feedback which is then connected to a waveform digitizer. The width of the waveform gives the drift time of the electrons. Equation 7 can also be written in the form:

$$\frac{\mathrm{Q_K}}{\mathrm{Q_A}} = \mathrm{e}^{-\mathrm{t}/\tau} \tag{9}$$

where Q_K is the charge collected in the cathode, Q_A is the charge collected in the

anode, t is the drift time of the electrons and τ is the electron lifetime

Let the ratio of the charge collected in anode to that in cathode be R

$$R = \frac{Q_A}{Q_K} \tag{10}$$

So lifetime of the electron τ will be

$$\tau = \frac{-t}{\log(R)} \tag{11}$$

2.2.3 TPC

The second phase of the Xenoscope involves the construction of the 1m Time Projection Chamber. As explained in the earlier sections, in a traditional xenon TPC the first signal (S1) is generated through scintillation, when a xenon atom is excited by particle interaction. However, in Xenoscope the primary signal is generated by flashing the photocathode by xenon lamp, identical to what is done in the first phase using purity monitor. In this phase, a liquid-gas interface will be introduced in the top, an extraction field will be applied to extract the drifting electrons to the gas phase. This will lead to the production of the secondary signal via electroluminiscence at the liquid-gas interface. To detect the secondary light signal, an array of Silicon Photomultipliers will be fixed on the top of the detector, as shown in figure 16. The array will hold 196 single detectors of dimension 6×6 mm^2 distributed in 12 tiles [3]. The proportional VUV light signal will be observed using an array of 48 VUV4 Multi Pixel Photon Counter (MPPC) of dimension 12×12 mm^2 installed in the gas phase. A 12×12 mm^2 'quad' detector is composed of four independent 6×6 mm^2 MPPCs. Sixteen of these MPPC channels are grouped into a single channel to form a 'tile'.

Reconstruction of an event is achieved by combining the information of the xenon lamp trigger, drift distance and the detection of the second signal by the top photosensor array. The amplification of the secondary signal depends on the strength of the extraction field applied between the liquid and the gas phase and also on the distance between the LXe level and anode. An extraction field of 10 kV/cm is applied and the liquid level is controlled using a weir system [3].

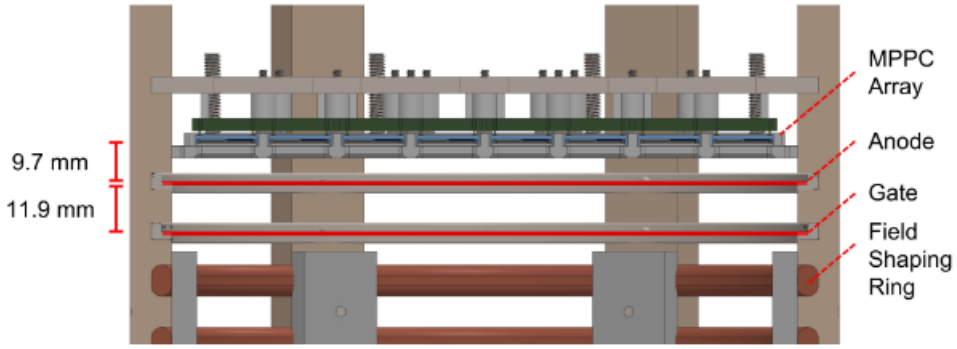

Figure 16: Drawing of the top section of the TPC where the placement of anode, anode grid and the MPPC array is shown. The distance between the MPPC array and anode is 9.7 mm whereas the distance between the anode and the anode grid(gate) is 11.9 mm [3].

For the final run, the full scale 2.6-m TPC will be used. In this phase, the photocathode will be biased at -50 kV which will produce a 190 V/cm drift field. This biasing will be done by a ceramic feedthrough that will enter the TPC via the bottom flange of the inner vessel [3].

3 Muon Detection

3.1 Cosmic Muons

Cosmic rays refer to high energy particles that travel through space until they reach the Earth's atmosphere. Cosmic rays consist of protons, alpha particles and of other heavier nuclei, which upon interacting with the molecules of the atmosphere produce secondary cosmic rays. These secondary cosmic rays consist mostly of pions and kaons. Neutral pions further decay into gamma rays and charge pions decay into muons and neutrinos. Muons are produced high in the atmosphere and lose about 2 GeV [25] energy as they travel before reaching the ground.

Cosmic ray muons have properties like charge and spin similar to those of electrons but are almost 200 times heavier than electrons. Muons are unstable particles with a lifetime of 2.2 μs. Muons can decay into electrons and neutrinos according to the following decay channels:

$$\begin{aligned} \mu^+ &\longrightarrow e^+ + \nu_e + \bar{\nu_\mu} \\ \mu^- &\longrightarrow e^- + \bar{\nu_e} + \nu_\mu \end{aligned}$$

Despite having a low lifetime, cosmic ray muons make it down to detectors at the surface of the earth because of the fact that muons travel close to the speed of light and therefore experience relativistic time dilation.

The mean energy of muons at sea level is ~ 4 GeV. The integral intensity of vertical muons (muons with zenith angle, zero degree) with momentum above 1 GeV/c at sea level is $\propto 70\,\mathrm{m^{-2}s^{-1}sr^{-1}}$ [25]. The overall angular distribution of muons at the ground as a function of zenith angle θ is proportional to $\cos^2(\theta)$, which is characteristic of muons with energy E $\sim 3\,\mathrm{GeV}$. This approximation is not valid for $\theta \geq 70$ degrees [25]. As the particles like cosmic muons interact with matter via radiative and collision processes, they lose energy. The probability of such interactions is given by their interaction cross section. Energy loss, also known as stopping power is defined as

-dE/dl where E is the kinetic energy of the interacting particle and l is the distance traversed by the interacting particle in the material. The higher the stopping power, the more the energy loss, and therefore shorter the range into the material the particle can penetrate. The negative sign expresses the loss of energy. As the energy loss is proportional to the material density, it is often scaled to the density ρ

$$-\frac{1}{\rho}\frac{\mathrm{dE}}{\mathrm{dl}} = -\frac{\mathrm{dE}}{\mathrm{dx}} \tag{12}$$

where $\mathrm{x} = \mathrm{l}\rho$. So, energy loss is often expressed in $\mathrm{eVcm}^2/\mathrm{g}$. After interacting with matter for a certain distance, the particle comes to rest as it loses all its energy. The well defined distance where the particle comes to stop is called range. The ways in which the particle interact with matter depends on the particle type and its energy. For charged particles the main mechanisms of energy loss are Bremsstrahlung, Cherenkov effect, radiation, ionization and excitation.

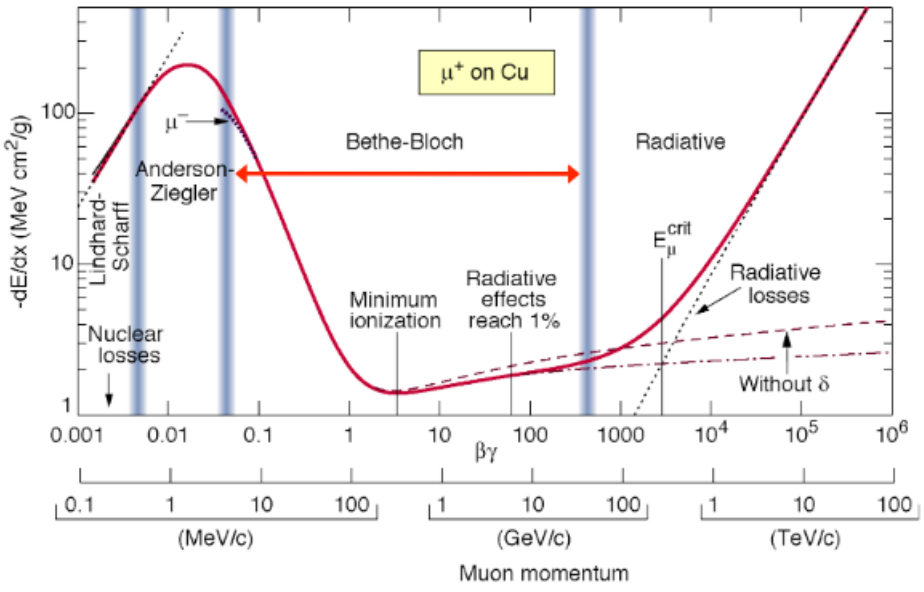

Figure 17: Stopping power (-dE/dx) for positive muons in copper as a function of their momentum $p = M\beta c\gamma$. The Bethe Bloch formula is valid for charged particles with intermediate velocities where the main mode of energy loss is through ionization. In the low velocity region, muon velocity becomes comparable to the electron velocity and for the high velocity region, radiation effects become important [26].

The mean rate of energy loss by moderately relativistic charged heavy particles, is well-described by the "Bethe Bloch" equation, [26]

$$-\frac{dE}{dx} = K_B z^2 \frac{Z}{A}\frac{1}{\beta^2}\left[\frac{1}{2}\frac{\ln(2m_e c^2\beta^2\gamma^2 T_{max})}{I^2} - \beta^2 - \frac{\delta(\beta\gamma)}{2}\right] \tag{13}$$

It describes the mean rate of energy loss for charged particles in the region $0.1 \leq \beta\gamma \leq 1000$. The validity range of the Bethe Bloch formula is indicated in the figure 17. There are two regions where the formula is no longer valid. At low velocities, when the muon velocity becomes small compared to the velocity of the electrons in the material and at high velocity, when the radiation effects become important. In the formula, K_B is the Maxwell- Boltzmann constant, z and M are the charge and mass of the incident particle (muon, in our case) respectively, Z is the charge number and A is the atomic number of the medium, β is v/c where v is the velocity of the charged particle and c is the speed of light, γ is $1/\sqrt{(1-\beta^2)}$ and $\beta\gamma = p/M$ where p is the momentum of the charged particle. δ is the density correction in the formula and I is the mean excitation energy of the medium. T_{max} is the maximum kinetic energy transferred to an electron in a single collision and is given by the formula [26]

$$T_{max} = \frac{2m_e c^2\beta^2\gamma^2}{1 + 2\gamma m_e/M + (m_e/M)^2} \tag{14}$$

The Bethe Bloch region can be further divided into different regions. The first region is for particles with low velocities , here the stopping power falls off $\propto \frac{1}{\beta^2}$. This is because of the fact that slower particles spend more time in the vicinity of the electrons. The velocities of such particles become comparable to the orbital electron velocities and shell correction has to be taken into account. While deriving the Bethe Bloch equation, the assumption of electrons being at rest is made and it is valid for particles with very high velocities as the electron velocity becomes negligible in comparison. But for particles in the low velocity region, corrections have to be made since the assumption is no longer valid. At $\beta\gamma \sim 3.5$, the stopping power reaches its minimum. The particles in this region are called minimum ionizing particles. After this, there is a logarithmic rise in the stopping power due to the fact that the electric field of the interacting particle increases proportional to (γ) when they reach relativistic velocities. As the field becomes stronger, the interacting particle can ionize atoms at larger distances and lose more energy as a result. Eventually the medium is polarized and shields the atoms at a larger distance from the effect of the electric field. This reduces the

contribution of such atoms to the energy loss of the interacting particle. This is the origin of the density correction term in the Bethe Bloch equation.

3.2 Muon Detectors

Muon detectors consisting of plastic scintillators, acrylic lightguides and photomultiplier tubes were used in the course of this experiment. In this section the working principle of such detectors and all of their components will be discussed briefly.

3.2.1 Plastic Scintillators

A scintillator is a material that exhibits the property of luminescence (emission of light), called scintillation, when excited by ionizing radiation. The method of scintillation is one of the oldest types of radiation detection. Historically, measurements of the scintillation were done using photographic films. Nowadays, these are replaced by Photomultiplier tubes that convert the light output to voltage pulses which are then processed. When a gamma ray interacts with the molecules of a crystal scintillator, they emit a pulse of light which is usually in the visible spectrum. Various types of sensitive photo-detectors are closely coupled to the crystal so that the photons produced can be converted into voltage pulses.
Plastic scintillators fall under the category of organic scintillators. In organic materials, fluorescence mechanism takes place when there is a transition between energy levels of a single molecule. The plastic detectors are made up of low atomic number material such as C, H, O, so the efficiency of such detectors is low due to low stopping power and light yield. Applications of plastic scintillators include tracking of charged particles and usage in fast neutron detection. Due to their faster decay times in the order of a few nanoseconds and low manufacturing costs, plastic scintillators have advantages over inorganic scintillators. For this experiment, the muon detectors will only be used to tag the muon events, making plastic scintillators an optimal choice.
In a plastic scintillator, when energy from a charged particle is absorbed, it excites the electron to a variety of excited states. At room temperature, all molecules of the scintillator are in the singlet state S_{00}. When the charged particle interacts with the molecules of the scintillator, its kinetic energy is absorbed by the molecule and they are excited to higher levels like S_2, S_3, as shown in figure 18. This is followed by de-excitation that occurs through internal conversion to the S1 state. This results in

the presence of a population of excited molecules in the S_{10} state. When the molecules transit from S_{10} state to the ground state S_{00}, they emit scintillation light [27].

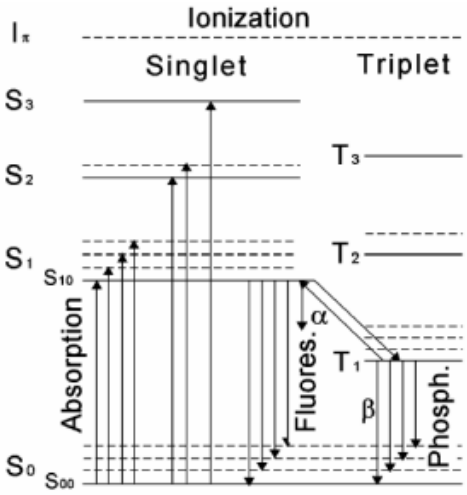

Figure 18: Energy levels in organic molecules. S_0 S_1 S_2 S_3 indicate the singlet states.The upward arrow shows the excitation of electrons from ground state to higher energy states whereas the downward arrow indicates the de-excitation of the electrons. The process of de-excitation is responsible for the emission of scintillation light [27].

Figure 19: Two BC-412 plastic scintillators made of Polyvinyl Toluene(PVT) used for the muon detectors. Plastic scintillators have a low decay time of a few nanoseconds making them the choice for our setup where the detectors will be used for tagging muon events.

Two BC-412 plastic scintillators, shown in figure 19, of dimensions $35.5 \times 5.3 \times 5.3\,\mathrm{cm}^3$ were used as the muon detectors. The density of the BC-412 scintillator material is

1.023 g/cm^3. BC-412 scintillators are generally used in large areas and long strips to detect 100 keV to 5 MeV gamma rays, fast neutrons, charged particles, cosmic rays, muons, and protons. The wavelength of maximum emission for BC-412 plastic scintillator is 434 nm [28].

3.2.2 Lightguide

Lightguides are used to couple the scintillators to the photo-detectors because often the geometrical shape of the scintillator does not match that of the photo-detector. The efficiency of light transmission through a light guide is limited by two factors: the angle of total reflection and the Liouville's theorem which states the conservation of phase space meaning the flux of photons per unit area per unit solid angle must be constant throughout the lightguide. Because of Liouville's theorem, no lightguide can transfer photons from a scintillator with large area to a PMT with a smaller area with full efficiency. Since the area of the scintillator is smaller compared to the PMTs used for the detectors in this case, the only factor limiting the efficiency of light transmission is the angle of total internal reflection. The light transmission is limited by total internal reflection (TIR). TIR is the process where the light rays are totally reflected when they reach the interface of two mediums. The condition of TIR allows the scintillation lightguide to travel inside the lightguide without being refracted out of the detectors.

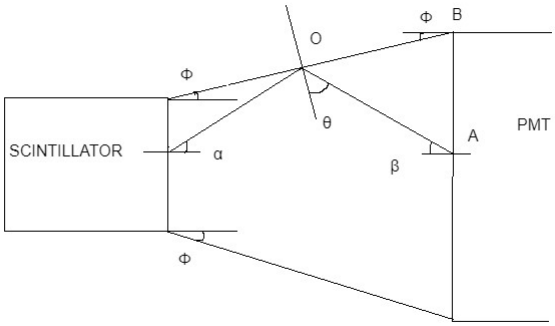

Figure 20: Sketch to explain the working principle of the lightguide. ϕ is the angle the lightguide is tapered with. The scintillation light enters the lightguide at an angle α, gets reflected fully at interaction point O if the criteria of TIR is fulfilled and leaves the lightguide at an angle β.

In Figure 20, α is the angle at which the photon enters from the scintillator to

the lightguide, it gets reflected from the interaction point O if the criteria for TIR is fulfilled. The criteria for TIR to take place is when the incident angle is greater than the critical angle which is defined as θ here. $\sin(\theta) \geq \frac{\mathrm{n_{ext}}}{\mathrm{n}}$ where n_{ext} is the refractive index of the external medium which in this case is air. So, $\mathrm{n_{ext}} = 1$ and n is the refractive index of the lightguide. This implies,

$$\sin(\theta) \geq \frac{1}{\mathrm{n}} \tag{15}$$

Considering triangle OAB,

$$(\pi/2 - \theta) + (\pi/2 - \phi) + (\pi/2 - \beta) = \pi \tag{16}$$

$$\beta = \pi/2 - \phi - \theta \tag{17}$$

Here , β is the angle at which the photon is emitted out of the lightguide and ϕ is the angle at which the lightguide is tapered. Since there is a lower limit for θ according to equation 15, this sets an upper limit to the angle at which light emits out of the lightguide β according to equation 17. The lightguide was to be designed in such a way that it connects the square surface of the scintillator to the circular surface of the PMT. For the lightguide to work smoothly, sharp kinks were to be avoided so it was tapered by a small angle of 11 degrees. The lightguide was fabricated by the workshop in the University of Zurich, shown in figure 21 . To get maximum light transmission , the critical angle should be lower which means a material with high refractive index should be used. This is the reason acrylic material whose refractive index is 1.495 was chosen.
Using equation 15, the critical angle comes out to be 41.9°.
As $\phi = 11°$. The maximum angle at the lightguide output will be 37.1° according to equation 17.

Figure 21: Lightguide fabricated by the mechanical workshop in the University of Zurich. It is made of acrylic material whose refractive index is 1.495. The lightguide is tapered at an angle of 11°.

3.2.3 Photomultiplier Tube (PMT)

Photomultiplier tubes are used to convert scintillation light into an electrical signal. A few hundred photons are required to generate electrical pulses. The working principle of PMTs is based on the photoelectric effect. When the photons from the scintillation light strike a photocathode of a PMT, they produce electrons if the energy of the photons is greater than the work function of the photocathode material. The rest of the photon energy is transferred to the electrons in form of kinetic energy. These electrons generated by photons, usually called photoelectrons, are then accelerated by a high voltage field inside the photomultiplier tube. The number of photoelectrons generated, depends on the quantum efficiency of the PMT which is defined as the ratio of the number of electrons generated to the number of incident photons. The photoelectrons are then multiplied in number by the presence of dynodes. Dynodes are electrodes which when hit by a primary electron with sufficient energy, produce multiple electrons from the molecules of their material which are called secondary electrons and the process is called secondary emission. These electrons are then collected by the anode. PMT bases are designed and used to distribute voltages to all the elements of the PMT required for its operation and also to extract signal from it. To divide the high voltage and provide it to each dynode, a voltage divider circuit with resistors is used as shown in figure 22.

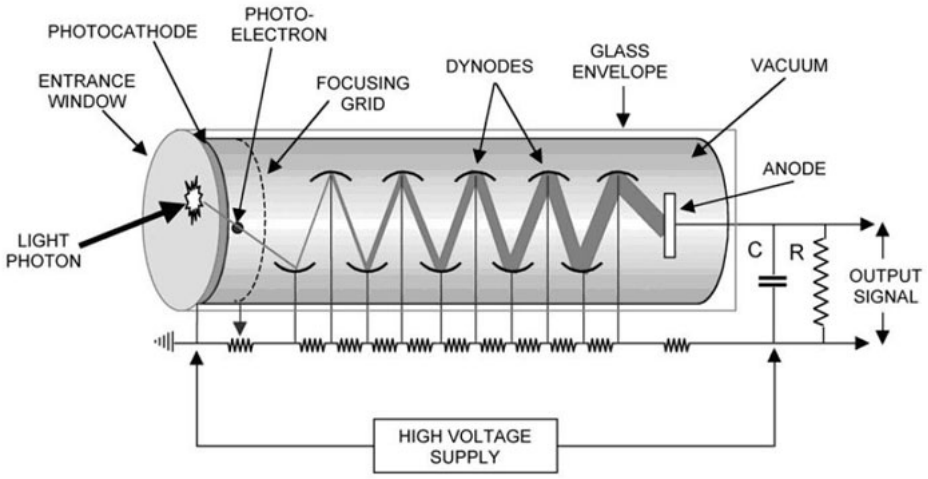

Figure 22: Sketch showing the working method of a photomultiplier tube. The photon produced in the scintillator travels through the lightguide and strike the photocathode of the PMT, producing electrons via photoelectric effect. The electrons then travel towards a series of dynodes and are finally collected at the anode, producing an output signal [29].

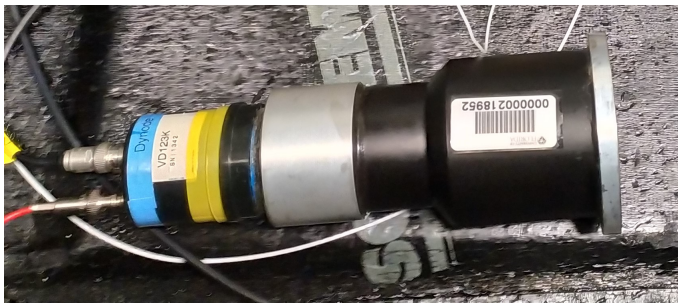

Figure 23: Photomultiplier tube used for the muon detectors. It has a photocathode area of 67.9 cm^2.

The PMTs must be powered with a negative high voltage supply and the signal can be read from the anode. For this experiment two PMTs were used with a photocathode area of 67.9 cm^2, shown in figure 23. The first step in characterizing the setup is to find an ideal voltage to operate the PMTs. This can greatly affect the amplitude of the pulses and therefore the count rate. A small change in operating voltage must not lead to a significant change in pulse amplitude for the two PMTs. To do this, the anode pulse for each detector was measured using an oscilloscope, shown in figure 24 while varying the supply voltages.

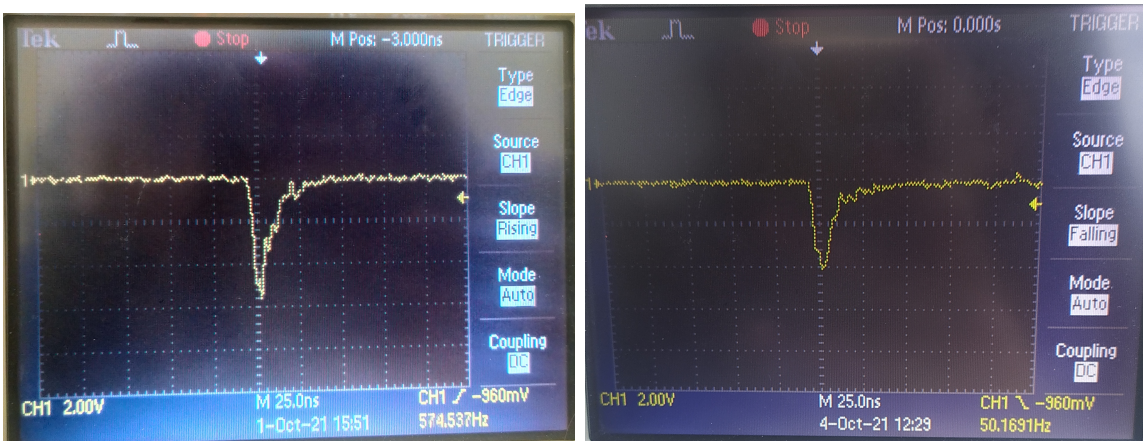

Figure 24: Output signal of the detector-2(left) and detector-1(right) as seen in the Oscilloscope when a high voltage of -2500 V is applied.Difference in the amplitude of the output signal from the two detectors show that the PMTs do not function identically.

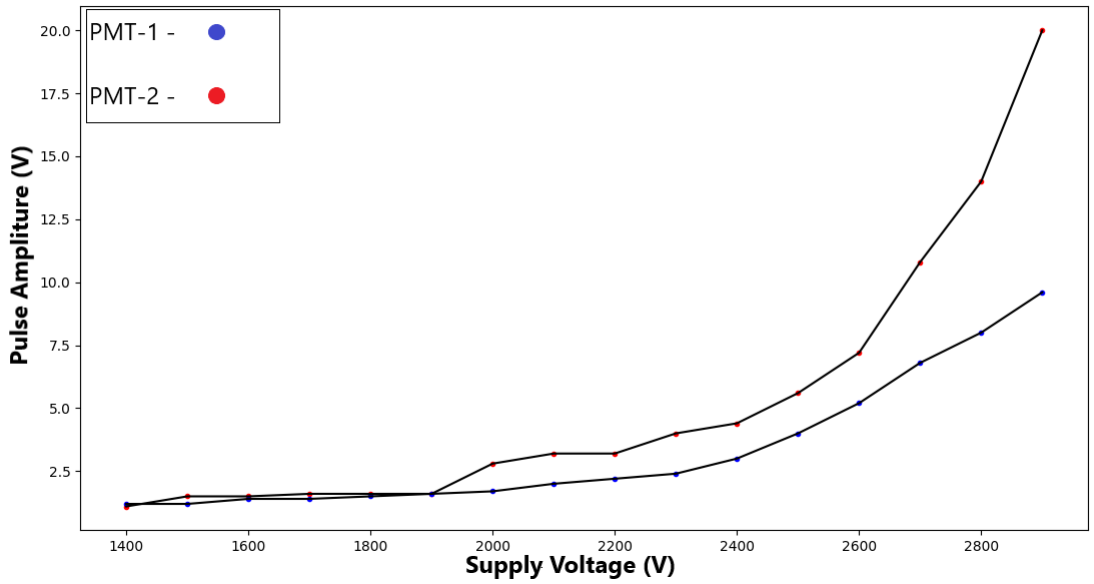

Figure 25: Variation of the amplitude of the output signal for the two PMTs with supply voltage. The pulse amplitudes begin to fluctuate more with a small change in voltage for supply voltages above 2500 V (negative polarity).

It is evident from the above plot that the two PMTs used do not function identically because the pulse amplitude varies from one PMT to the other for a given supply voltage. Figure 25 shows that we should avoid operating the PMTs at above 2500 V (with a negative polarity) as pulse amplitudes vary greatly with small changes in

supply voltage in this region. In addition to this, the manual for the PMTs used suggested the use of the PMTs at -2500 V for optimal results.

3.2.4 Assembly

All the three components of the detector were fixed together using clamps that were custom designed and fabricated by the mechanical workshop at the University of Zurich. Four sets of square clamps, shown in figure 26 to connect the scintillator and the lightguide and two sets of circular clamps, shown in figure 27 to connect the lightguide and the PMT were produced . In addition to the clamps, dow corning (DC) electrical insulating compound (EIC) 4 silicon grease was also used between the components for better coupling as it adheres easily to dry metals, ceramics, rubber, plastics and insulating resins. It is a grease-like material containing an inert silica filler in combination with selected ploydimethyl silicone fluids. It retains its grease-like consistency from -55 C to +200 C [30]. Figure 28 shows the assembly of the three components using the connectors.

Figure 26: Rectangular clamps fabricated by the mechanical workshop of the University of Zurich to couple the lightguides to the scintillators.

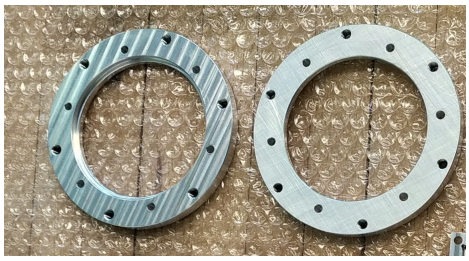

Figure 27: Circular clamps fabricated by the mechanical workshop of the University of Zurich to couple the lightguide to the PMT.

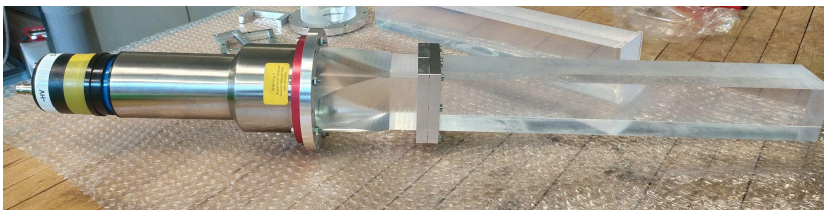

Figure 28: All the three components of the detectors (scintillator,lightguide and PMT) assembled using the clamps.

Applying reflectors on the scintillator surface has proved to increase the light extraction efficiency by decreasing the light losses. In current radiation detectors based on scintillators, one of the most commonly used techniques to overcome the light losses consists of the use of teflon wrapping. So, the scintillator and the lightguide in the muon detectors were wrapped with teflon tape, shown in figure 29. If the detectors are not covered by any material, the scintillator can let light escape through its lateral surfaces, losing a significant amount of optical photons. It was ensured that the scintillator and lightguide surfaces were cleaned and free of marks and fingerprints before two layers of teflon tape were wrapped around them.

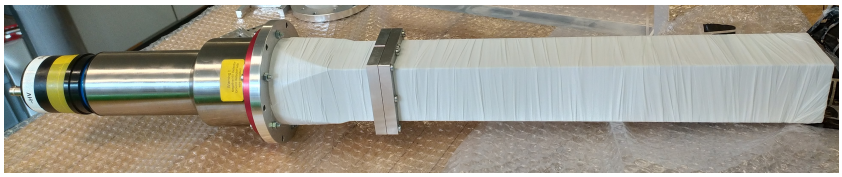

Figure 29: The assembled components were wrapped with two layers of teflon tape to limit the light loss so that maximum scintillation light travels to the Photocathode of the PMT.

To make the detector light tight, it was then wrapped with black electrical tape, shown in figure 30.

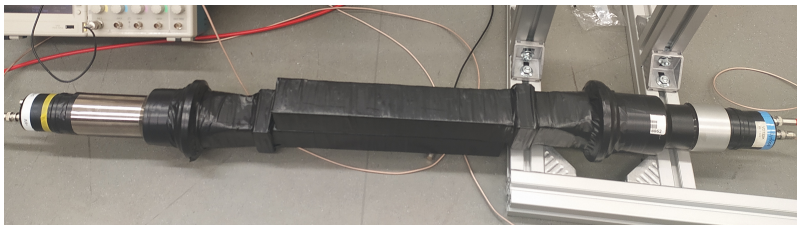

Figure 30: The two muon detectors after being wrapped with black electrical tape to seal them off from light.

3.3 Support Structure for muon detectors

To run the experiment and make the measurements, the muon detectors were to be fixed to the inner frame around the cryostat of Xenoscope containing the purity monitor. For this purpose, we came up with a design of the support structure to hold the muon detectors, as shown in figure 31. The support structure was assembled using 50×50 mm^2 aluminium profiles. Two thin aluminium plates were attached to the profiles to hold the muon detectors. These support structures were then attached to the inner frame at the Xenoscope facility.

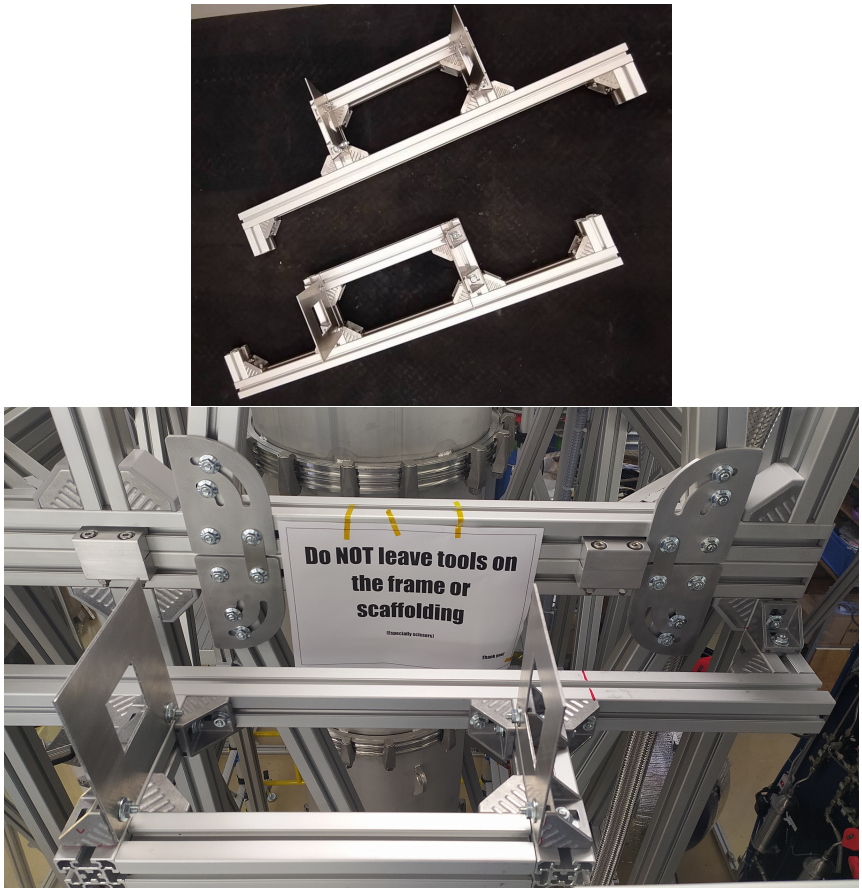

Figure 31: (top) Frame for the detectors assembled using aluminium profiles. (bottom) Frame of the detectors attached to the inner frame of the demonstrator. The cut outs in the two aluminium plates allow the muon detectors to be fixed properly.

3.4 Detection of Muons

As already mentioned in the beginning of this chapter, cosmic ray muons have an average energy of approximately 6 GeV upon creation and 4 GeV at sea level. The energy loss between these two points is mainly due to interaction with air molecules in the atmosphere. This implies that the peak of muon energy distribution would shift towards lower energies with decreasing altitude. The plastic scintillators that are used in this experiment are made up of Polyvinyltolulene (PVT) and have a dimension of $35.5 \times 5.3 \times 5.3\,\mathrm{cm}^3$. It has $\frac{Z}{A}$ ratio of 0.54155. Using the Bethe Bloch equation, the $\frac{Z}{A}$ ratio and the mean excitation energy of PVT, the stopping power of muons in PVT is plotted as a function of muon momentum in figure 32.

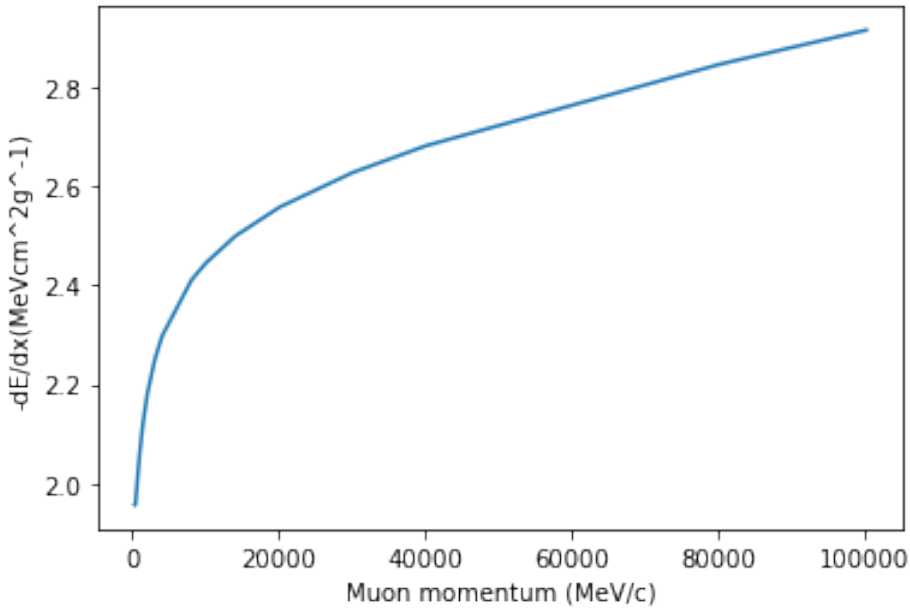

Figure 32: The stopping power of muons in PVT as a function of muon momentum ranging from 300 MeV/c-100 GeV/c. Bethe Bloch formula is used for this plot.

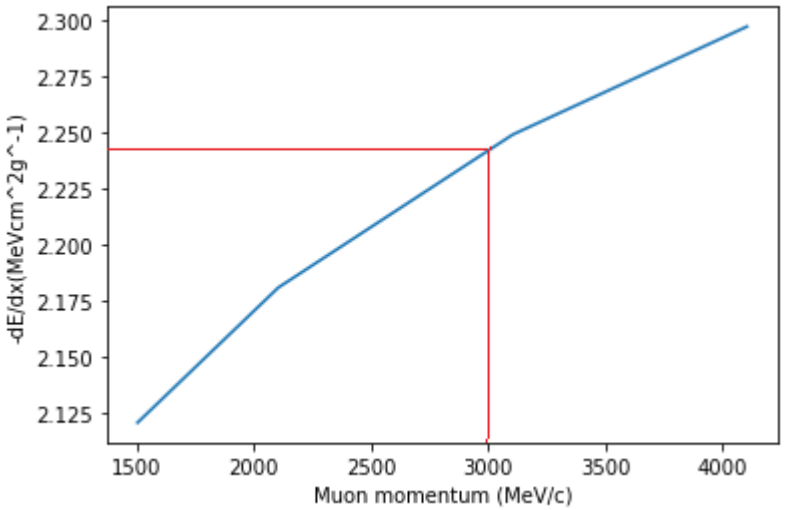

Figure 33: Stopping power of muons in PVT plotted against their momentum in the region 2-4 GeV/c. This is the region of or interest since the average energy of muons at sea level is $\sim$ 4GeV.

$\left(\frac{Z}{A}\right)_{PVT}$	0.54155
ρ_{PVT}	1.032 g/cm^3

To calculate the energy deposited by 3 GeV muons in the plastic scintillator,

$$\left(\frac{dE}{dx}\right)_{PVT} = 2.249\,\text{MeV}\,\text{cm}^2/\text{g} \tag{18}$$

which is calculated using the Bethe Bloch formula and is also marked in figure 33.

$$\frac{dE}{dx} = \frac{1}{\rho}\frac{dE}{dl} \tag{19}$$

$$\text{So,}\left(\frac{dE}{dl}\right)_{PVT} = 2.32\,\text{MeV/cm} \tag{20}$$

The thickness of the plastic scintillator is 5.3 cm . Therefore, the energy loss of one muon in the plastic scintillator becomes, $dE = 2.32 \times 5.3\,\text{MeV} = 12.296\,\text{MeV}$

4 Measurements

4.1 Test measurement

Before designing our own muon detectors, the detectors that were already available at one of the student laboratories in the University of Zurich were used to create and test a double coincidence set up using the Nuclear Instrumentation Module (NIM). The dimensions of the scintillators in these detectors were $100 \times 40 \times 1$ cm^3. For the set up, two muon detectors were used. They were placed 70 cm apart. The area of the scintillator squares used for the muon detectors, shown in figure 35 were 4000 cm^2. A coincidence measurement was set up using NIM where a simultaneous hit in both the detectors within a coincidence window of 40 ns set by the CAEN logic unit acted as a trigger . A schematic of the measurement is shown in figure 34. A high voltage of -1100 V was applied to the PMTs. Signals from both detectors were sent to the amplifier; the amplified signals were in turn sent to a discriminator where the discriminator threshold ensured the collection of muon events. The signals with amplitude above the set discriminator threshold then went to the CAEN logic unit, where the double coincidence was ensured using the AND logic gate. The output signal from the logic unit was used as a trigger for the DAQ CAEN v1730 and the signals from both the detectors were collected. We could finally see the muon events in the computer screen. The data was acquired overnight for 15 hours. The event rate (the number of double coincidence hits) acquired from this setup was 12 events per second. We also calculated the event rate using the muon flux formula to compare it with the experimental value. The flux of muons at the Earth's surface is given by the formula :

$$\frac{\mathrm{dN}}{\mathrm{dAdtd}\Omega} = \mathrm{I}_0 \cos^2(\theta) \tag{21}$$

where θ is the zenith angle of the incident muon. As the detectors were placed horizontally, muons with a zenith angle ranging from 0° to 90° could hit the detector. To take all the muons into account, the total flux should be the integrated flux with

respect to the zenith angle from 0° to 90°.

$$\frac{\mathrm{dN}}{\mathrm{dtdAd}\Omega} = \mathrm{I}_0 \int_0^{90} \cos^2(\theta)\mathrm{d}\theta \tag{22}$$

I_0 is the flux at zenith angle 0°. I_0 is $0.007\,\mathrm{cm}^{-2}\mathrm{s}^{-1}\mathrm{sr}^{-1}$ [?], dA is the surface area of the scintillator and dΩ is the differential solid angle.
The solid angle is calculated using [31],

$$\Omega = 4\arccos\sqrt{\frac{1+\alpha^2+\beta^2}{(1+\alpha^2)(1+\beta^2)}} \tag{23}$$

where $\alpha = \frac{\mathrm{a}}{2\mathrm{d}}$, $\beta = \frac{\mathrm{b}}{2\mathrm{d}}$, a and b are the sides of the rectangular surface, d is the distance between the two detectors and a is the area of the scintillator. The solid angle between the detectors was calculated to be 0.63 sr.

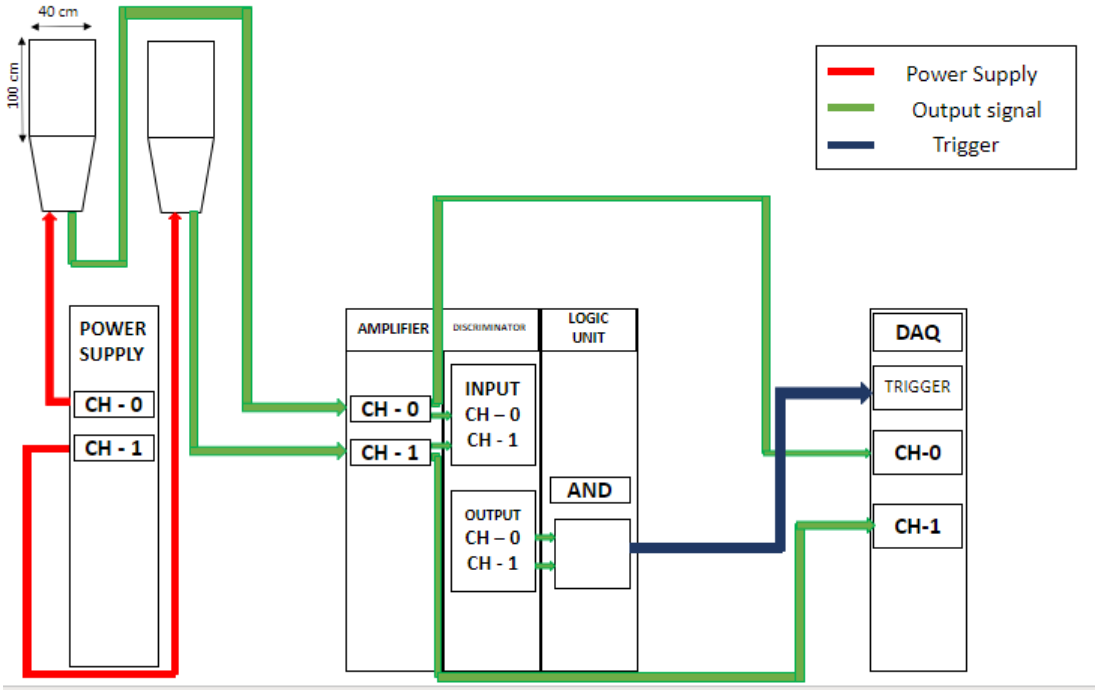

Figure 34: Schematic of the double coincidence setup for the muon detectors with dimensions 100 cm × 40 cm × 1 cm. The output from the detectors were sent to the Logic unit through the amplifier and discriminator, where double coincidence was ensured by the AND logic unit. The output from the logic unit was used to trigger the data acquisition system.

By using the value of I_0 and solving equation 22, the muon flux comes out to be,

$$\frac{dN}{dtdAd\Omega} = 0.00549$$

Substituting the value of $d\Omega$ obtained from equation 23 and the value of the surface area of the detectors , dA = 4000 cm^2, the event rate ($\frac{dN}{dt}$) becomes 13.8 events per second. The experimentally measured event rate comes out to be lower compared to the event rate calculated using the muon flux formula. The inefficiency of the detectors to detect very high energy muons that are taken into account in the muon flux formula can be one reason of this discrepancy.

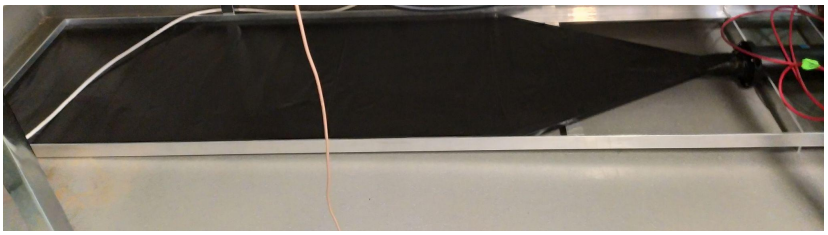

Figure 35: Muon detector used for test measurements with surface area dimension 100 cm × 40 cm. These detectors were placed 70 cm apart for the measurement.

4.2 Double Coincidence Measurement

After using the muon detectors from the student laboratory to check for the muon events, a double coincidence measurement for muons was set up with the newly assembled detectors using NIM electronics. Figure 36 shows a schematic overview of the double coincidence set up. The pulses obtained from PMTs were sent to a discriminator through an attenuator, in order to obtain a fast logic signal. In this experiment, a CAEN 8 channel leading edge discriminator (N840) was used. The role of the discriminator is to output a negative pulse of desired width and constant amplitude for every input pulse that exceeds a certain threshold, which can be set. The two discriminator outputs were then sent to a CAEN Quad Coincidence Logic Unit (N455). Using the push buttons, the logic gate can be set to OR or AND. For the double coincidence measurement, it was set to AND. The output pulse was also a fast logic signal, with a width equal to the overlap of the coincident input pulses. The output of the coincidence unit was sent to a CAEN 8 channel 14-bit digitizer to be used as a trigger for the channels with input signals from the detector PMTs. It then

displays on a screen the number of fast logic pulses received in a given amount of time.

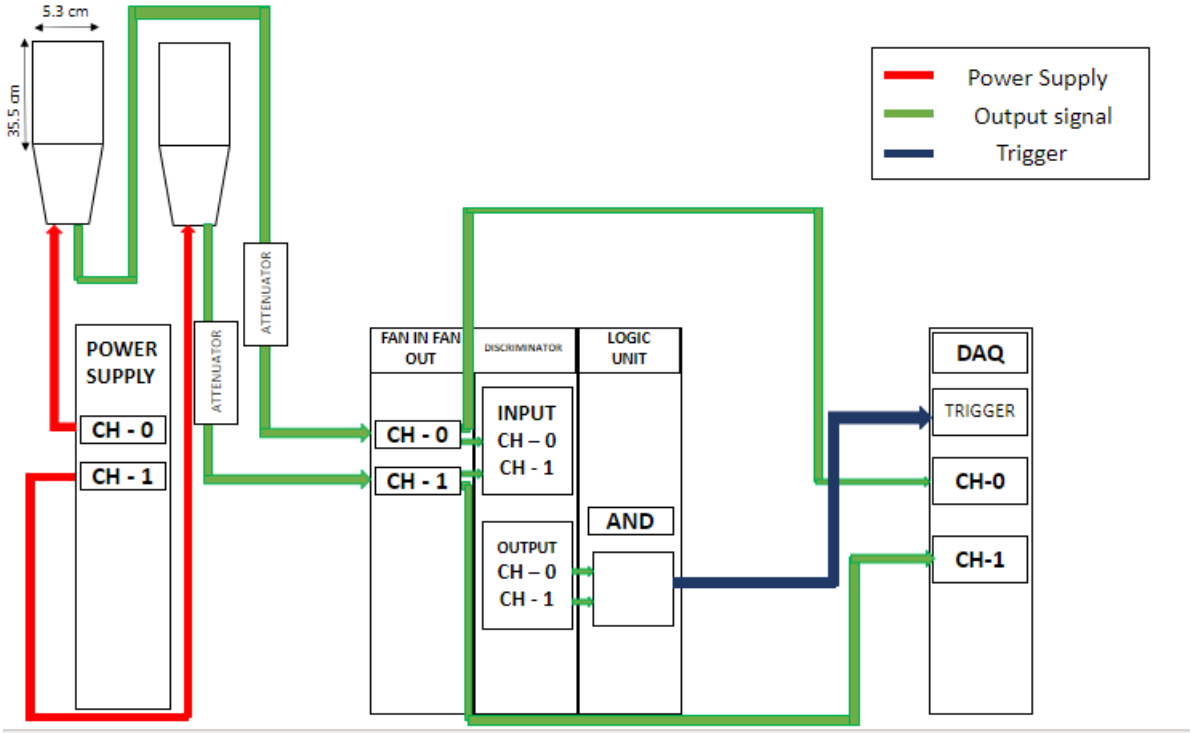

Figure 36: Schematic of the double coincidence setup for the muon detectors of dimensions 35.5cm × 5.3cm × 5.3cm. The output from the detectors were sent to the Logic unit through the attenuator and discriminator, where double coincidence was ensured by the AND logic unit. The output from the logic unit was used to trigger the data acquisition system.

4.2.1 Discriminator Threshold

A standard gamma source is usually used for the energy calibration of a general radiation detector. For these gamma sources in energy range 100 keV - 5 MeV, their spectrum in plastic scintillation detectors primarily reflect Compton scattering. Gamma rays usually scatter only once before exiting the detectors and rarely react to photoelectric absorption. The constituents of plastic scintillators are mainly low atomic number elements such as hydrogen and carbon. The probability that the gamma ray will interact with the material via photoelectric effect depends heavily on its atomic number, the overall dependence varies approximately as the power law. The Compton scattering probability also depends on the atomic number but it is a linear dependence. So when gamma rays interact with plastic scintillation detectors, Compton

scattering dominates among the three ways of interactions : Photoelectric absorption, Compton scattering and Pair production, as shown in figure 37. Compton scattering is the dominant form of gamma ray interaction in these detectors because of the low atomic number of the constituents of the scintillators, the geometry of the detectors constraining the number of times gamma rays scatter before exiting the detector and because of the fact that, in the energy range 100 keV - 5 MeV Compton scattering dominates among the other ways gamma rays interact with matter. Measurements of the Compton edge spectra using gamma sources were possible in this study.

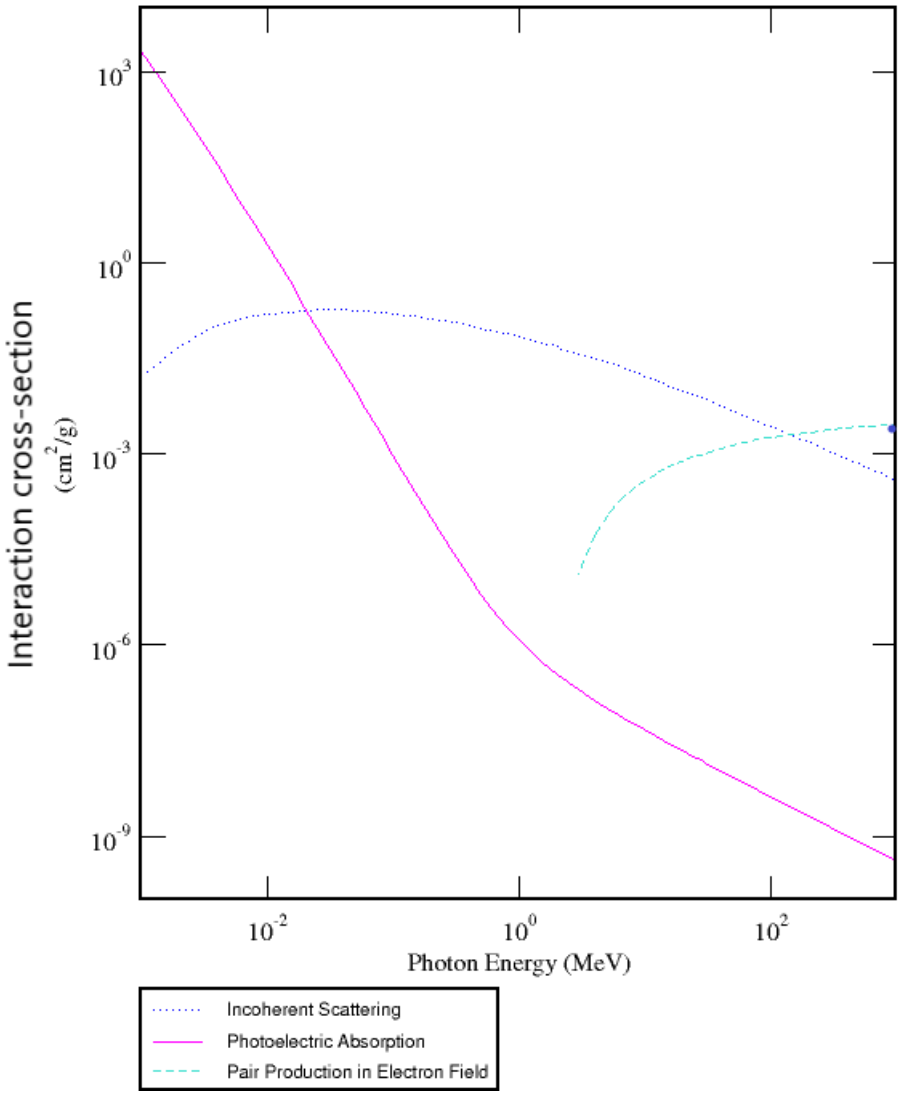

Figure 37: Interaction cross section of different photon interaction processes for Polyvinyl Toluene (C9H10) as a function of photon energy. The interaction process of Compton scattering dominates in the photon energy range of approximately 100 keV - 100 MeV [32].

In Compton scattering, a gamma ray is scattered by a free electron. The energy of the electron is transferred to the detector while the scattered gamma ray escapes from the detector. The energy of the scattered gamma ray is given by :

$$h\nu^{'} = \frac{h\nu}{(1 + h\nu/m_0c^2(1 - \cos\theta))} \tag{24}$$

The recoil electron has a well defined maximum energy (the Compton edge), which corresponds to the maximum transferred energy from the gamma ray to the electron. This maximum transfer of energy to the electron occurs when the angle between the incident gamma ray and the scattered gamma ray θ is π. At this angle, according to the Compton scattering equation given above, the energy transfer between the incident and scattered gamma ray is minimum. This edge can be used for the energy calibration of the detector and for comparing the relative light output from each scintillator.

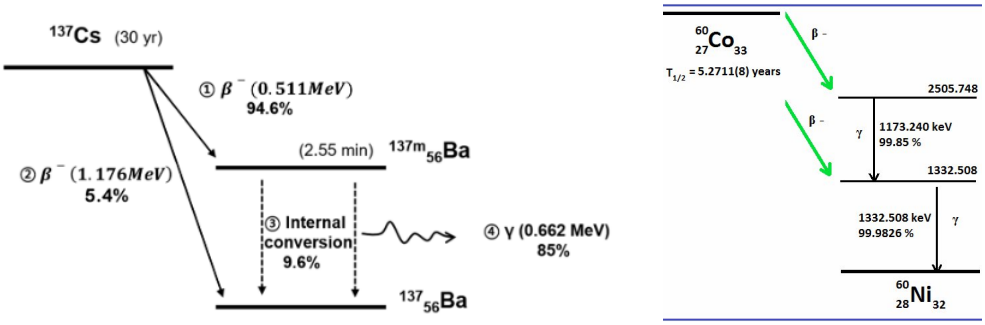

Figure 38: Decay diagram of ^{137}Cs (left) [33] and ^{60}Co (right) [34]. ^{137}Cs undergoes beta decay to Barium-137. 94.6% of these decays lead to the meta-stable state of ^{137}Ba which then decays back to its ground state by releasing a photon of energy 661 keV. Similarly, ^{60}Co decays to an excited state of ^{60}Ni which emits two gamma rays (1173 keV, 1332 keV) to reach the ground level.

In this work, two radioactive sources, ^{60}Co and ^{137}Cs were used to check the energy spectrum of the detectors in the presence of radioactive sources. The sources were placed on the detector surface in the middle of the scintillator. The anode signal from each of the PMTs was connected to the CAEN v1724 digitizer. The high voltage of the photomultipliers was set to -2500 V. The decay diagram of the two sources are shown in figure 38. The Compton edges for ^{60}Co and ^{137}Cs are 800 keV and 477.34 keV respectively and the photopeaks are at 1173 keV, 1332 keV and 661.66 keV [33] [34]. Due to the poor energy resolution of most of the Plastic scintillator detectors, the two peaks of ^{60}Co could not be seen. We looked at the background spectrum

for both the detectors and also the spectrum for these two radioactive sources. The different spectra that we got are shown below. The signals are shown in yellow and the area of the signal, which is directly proportional to the energy spectrum is shown in pink. The x axis of the plots is the voltage (mV) which is a measure of the area of the signal and the y - axis shows the number of counts. Since the output is a negative pulse, the area of the signal is given by negative voltage. The peak at the right most side of the spectrum is because of random fluctuations and noise which shows the low energy part of the spectrum. Comparing the background signal to the signals with the radioactive sources, a clear increase in the amplitude of the signals and a peak in the area spectrum at -165 mV for the third plot and -194 mV for the second plot in figure 40 can be seen indicating the presence of ^{60}Co and ^{137}Cs peaks respectively. The background spectrum for both the detectors were also recorded for 1800 s using the data acquisition system and compared as shown in figure 41. The small difference in the spectrum comes from the difference in efficiencies of the detectors which may have resulted from the different quantum efficiencies of the photocathode material or from the wearing out of dynode material of the PMT.

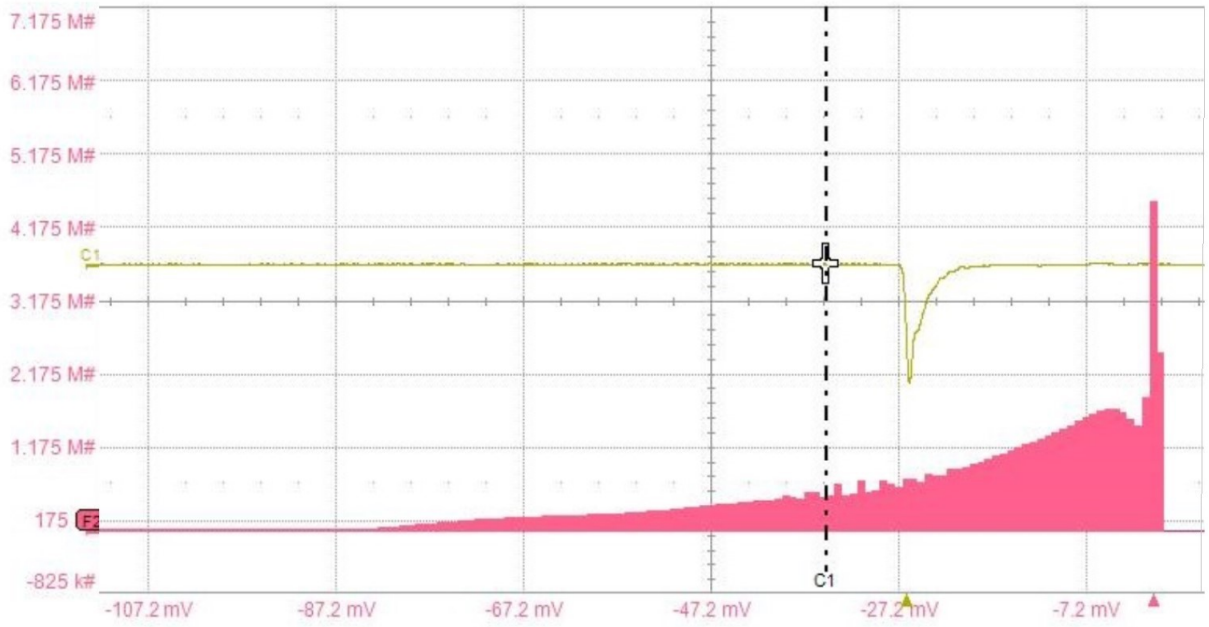

Figure 39: Comparison of the background spectra of Detector-1 and Detector-2. The nonidentical functioning of the two PMTs used for the detectors is one of the reasons for the difference in background spectrum of the two detectors.

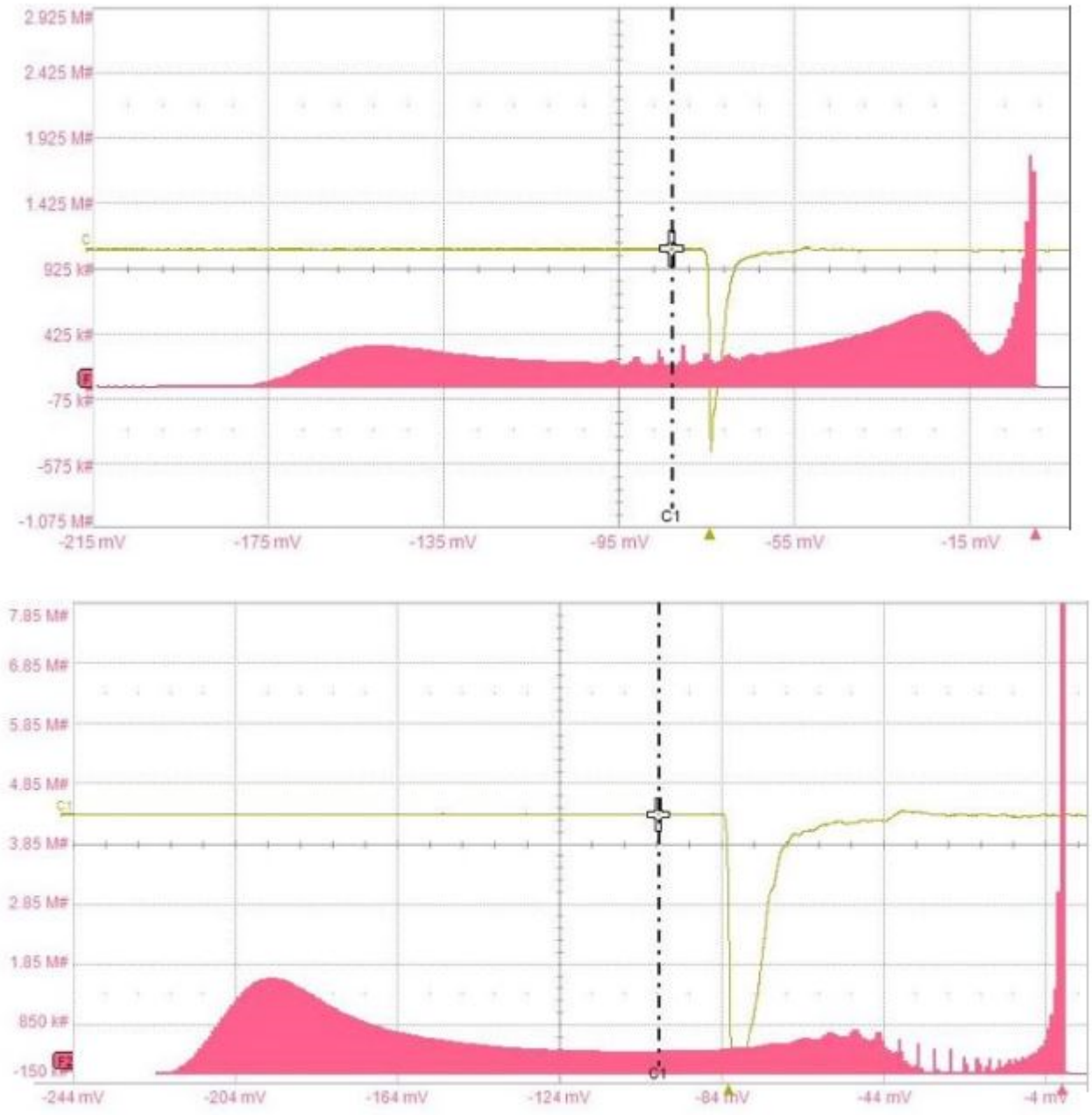

Figure 40: Background spectrum (top), spectrum with ^{137}Cs (middle) and spectrum with ^{60}Co (bottom) of Detector-1 recorded using the oscilloscope. The output signal is shown in yellow and the histogram in pink is for the area of the output signal which is a measure of the energy deposited by the interacting particle. The right most side of the histogram denotes the low energy part of the spectrum.

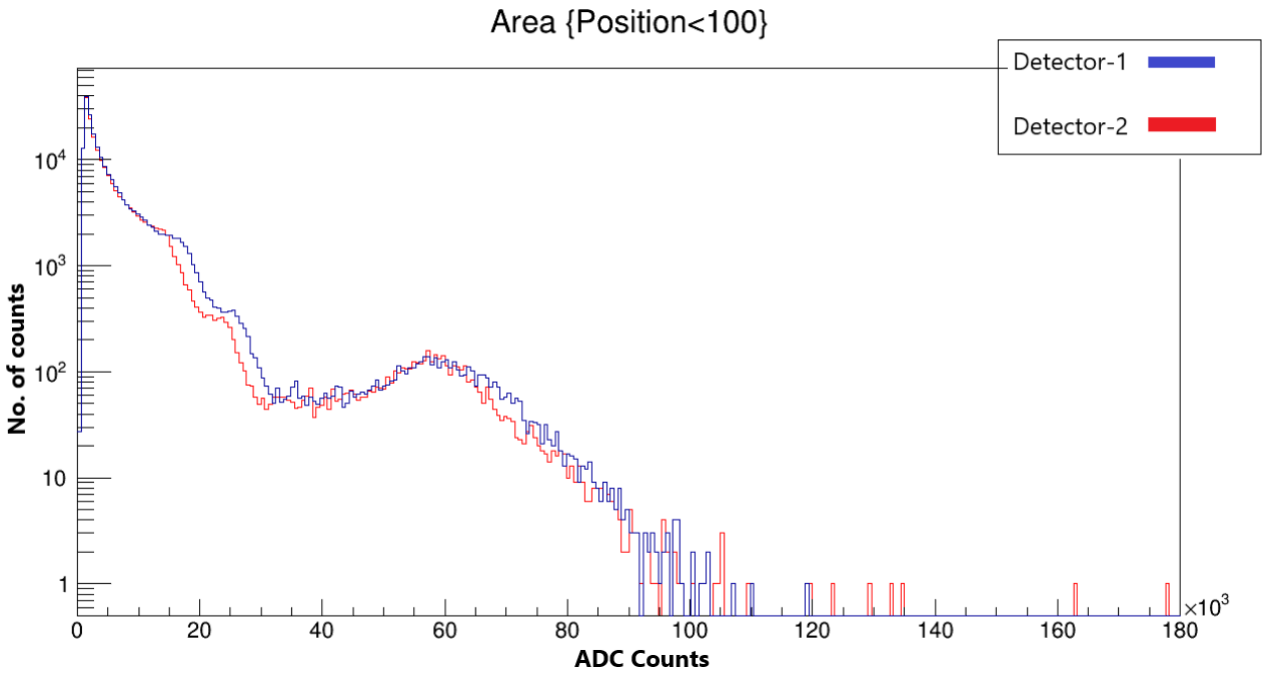

Figure 41: Comparison of the background spectra of Detector-1 and Detector-2. Events were recorded for 1800s for each detector. A position cut at 100 ADC count was made while processing the events to discard noise. The nonidentical functioning of the two PMTs used for the detectors is one of the reasons for the difference in background spectrum of the two detectors.

The threshold for the discriminator determines which raw detector pulses will produce logic units when passed through the discriminator and therefore how many events will be registered in the DAQ. If the threshold is too low, random fluctuations and electronic noise will be counted as muon events, but if it is too high, a large portion of muon events will be ignored.

As discussed in the previous chapter, the energy deposited by muons in the plastic scintillators detector is 12.29 MeV. The energy range for muons is much higher compared to the energy range of ^{60}Co source. The peak for the ^{60}Co source is at -210 mV, as seen in figure 40. Setting the discriminator threshold above 210 mV will cut out noise and low energy gamma events without cutting out any real muon events. Since the threshold settings of CAEN 8 channel leading edge discriminator (N840) goes up-to -255 mV, the threshold was set at -255 mV for the course of this study. Probability of recording noise or low energy gamma background is also reduced when the data is taken with a double coincidence trigger.

As mentioned earlier, the plastic scintillator material used for this experiment is BC-412 which is made up of Polyvinyl toluene. The BC-412 scintillator can detect charged

particles like muons and gamma rays within the energy range of 100 keV - 5 MeV but it cannot detect high energy gamma rays with energy greater than 5 MeV. The background for very high energy gamma rays become negligible because of this reason.

In order to reconfirm the discriminator threshold settings, double coincidence events were recorded while varying the threshold from 10 mV to 250 mV (negative polarity) at an interval of 10 mV while the separation angle was at 35°. Figure 42 shows the results of this set up.

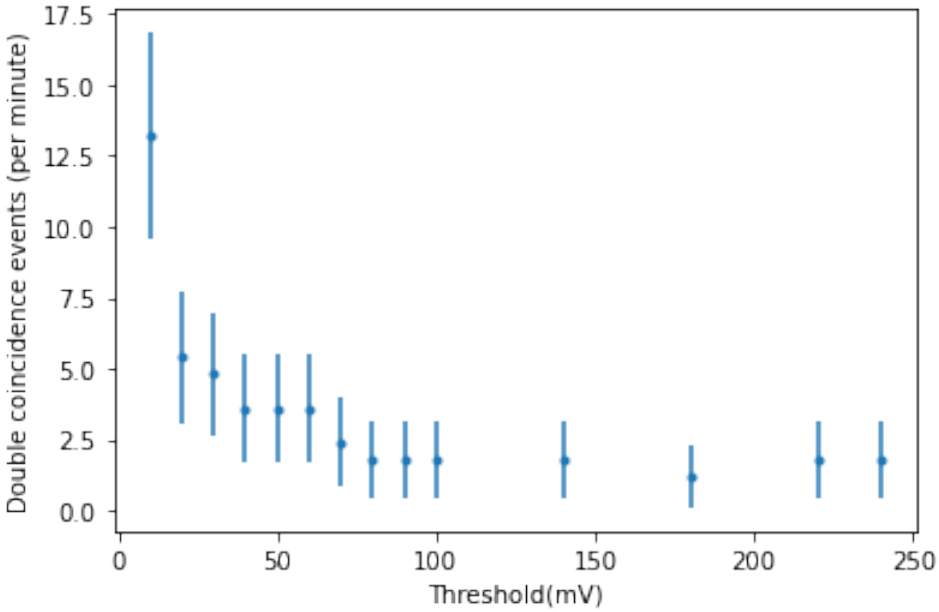

Figure 42: Relation between double coincidence event rate, where simultaneous hits in both the detectors within a coincidence window of 40 ns was considered an event and the discriminator threshold with an uncertainty of $\sqrt{n}$ where n is the event rate.

For the next set set of measurements, the ^{60}Co source was placed near detector-1 and double coincidence events were recorded while varying the threshold, the same was repeated while the source was placed near detector-2 . The results are shown in figure 43. This was done to check the effect of the source on the double coincidence event rate.

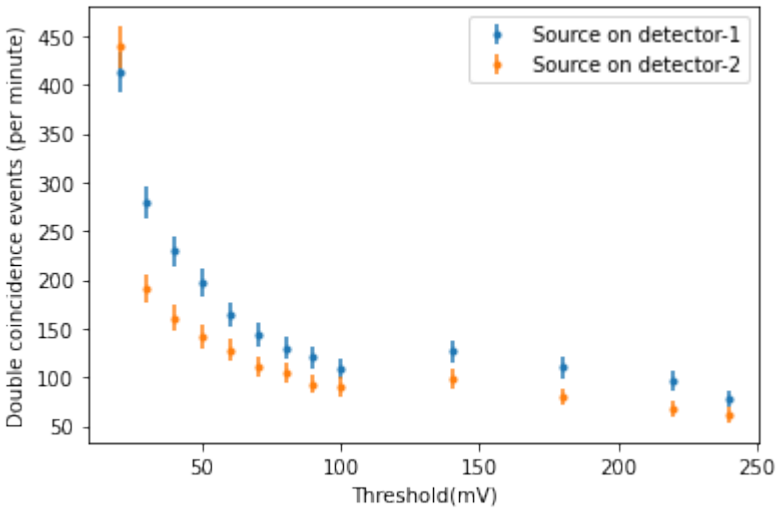

Figure 43: Variation of double coincidence event rate with discriminator threshold in the presence of ^{60}Co source near each one of the detectors with an uncertainty of $\sqrt{n}$ where n is the event rate.

The ^{60}Co source was also placed in between the two detectors and double coincidence event rates were recorded to get an estimate on the accidental coincidences. These are the hits that come from two different events but manage to deposit energy in the detectors within the coincidence window of the logic unit. The probability of having such accidental coincidence increases when a source is placed in between the detectors.

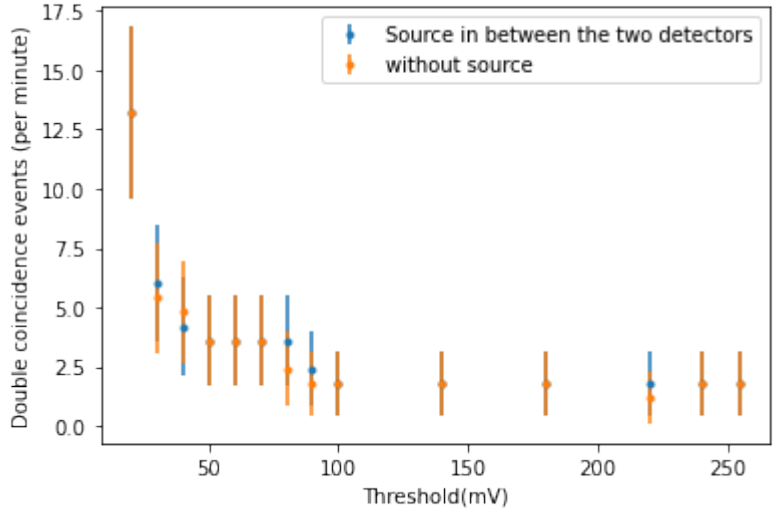

Figure 44: Relation between double coincidence event rate and discriminator threshold when the ^{60}Co source is placed between the two detectors.

As it can be seen from the plots, when a source is placed near one of the detectors,

the double coincidence event rate increases, whereas the shape of the plots remain same. Placing a source in between the detectors increases the accidental coincidence rate but as it can be seen from figure 44, the accidental double coincidence rate even with a source is low and comparable to the background. The probability of recording two hits (>255 mV) from two different events in the coincidence window of the logic unit is in the range 10^{-11} events. The probability of counting a gamma ray event instead of a muon event decreases after taking double coincidence measurement into account.

4.2.2 Muon Events Selection

Even after setting the discriminator threshold, there will be some gamma rays that deposit high enough energy in both the detectors to pass through the discriminator threshold. To eliminate such events, width and height cuts are made during the analysis. As shown in figures 46 and 48, all the events with width < 40 ADC counts and Height < 10000 ADC counts were excluded from the final analysis. Almost 40% of the total events recorded were excluded after this analysis.

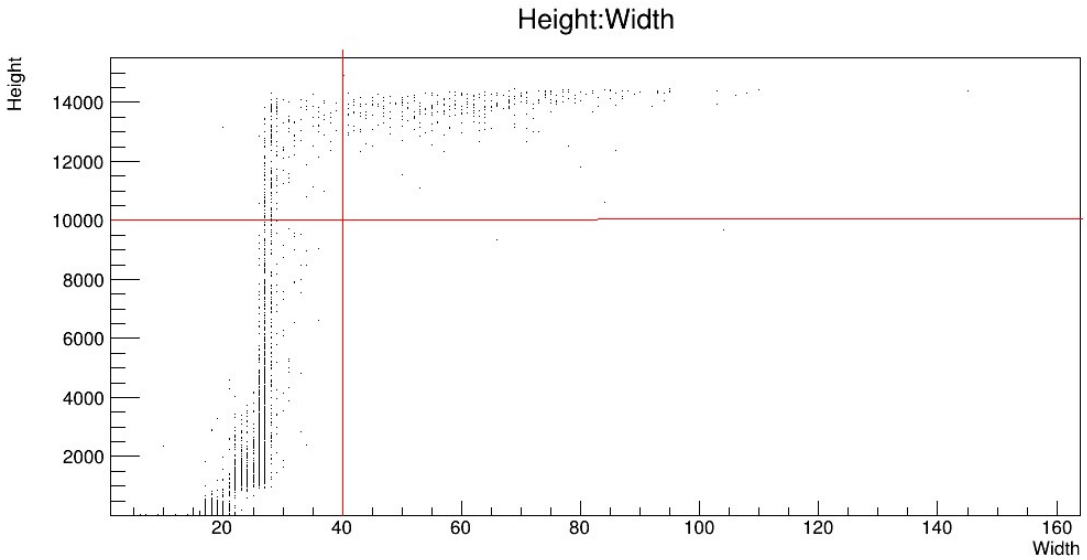

Figure 45: cuts made on the width and height of the signals recorded using detector-1 at 0° separation angle.

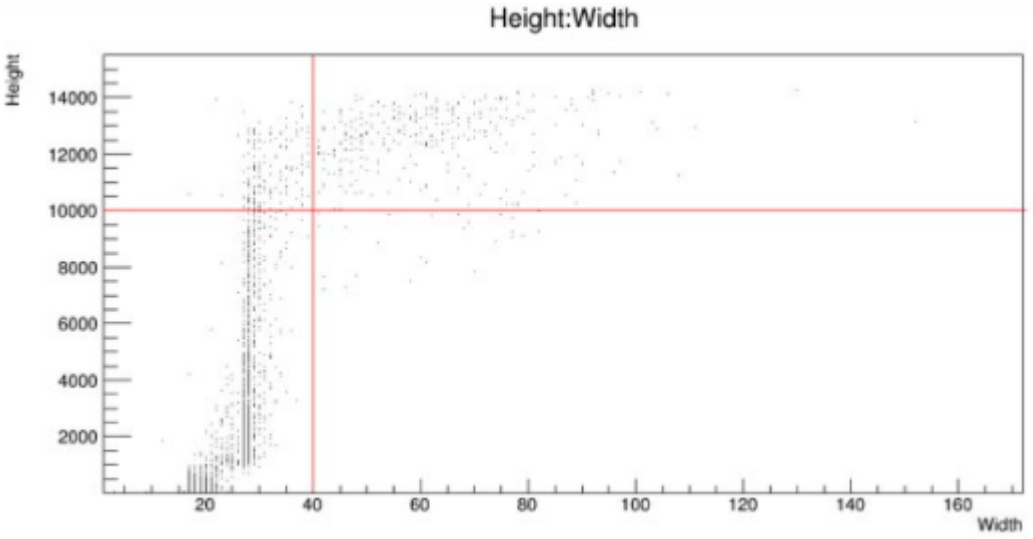

Figure 46: cuts made on the width and height of the signals recorded using detector-2 at 0° separation angle.

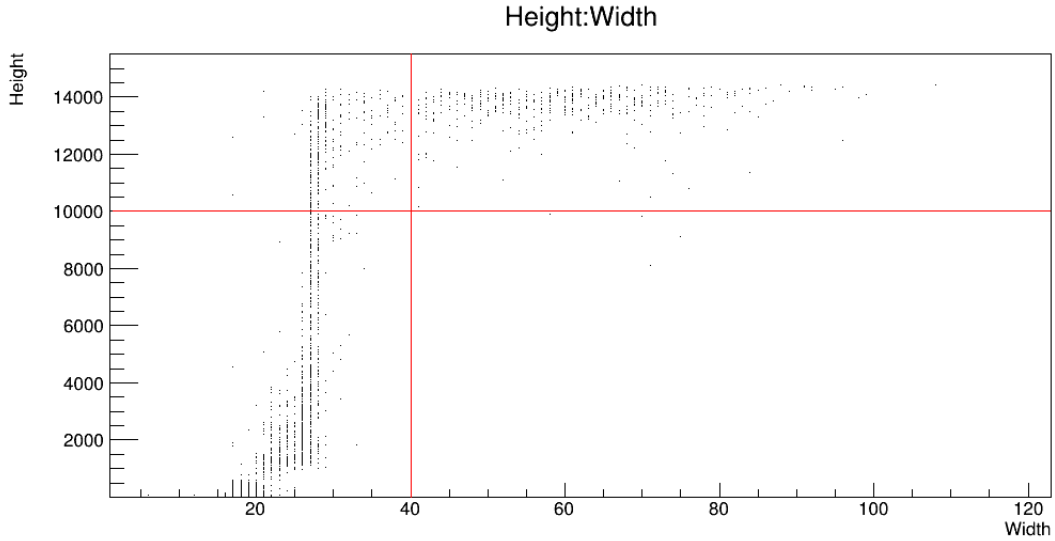

Figure 47: Plot showing the cuts made on the width and height of the signals recorded using detector-1 at 33 ° separation angle.

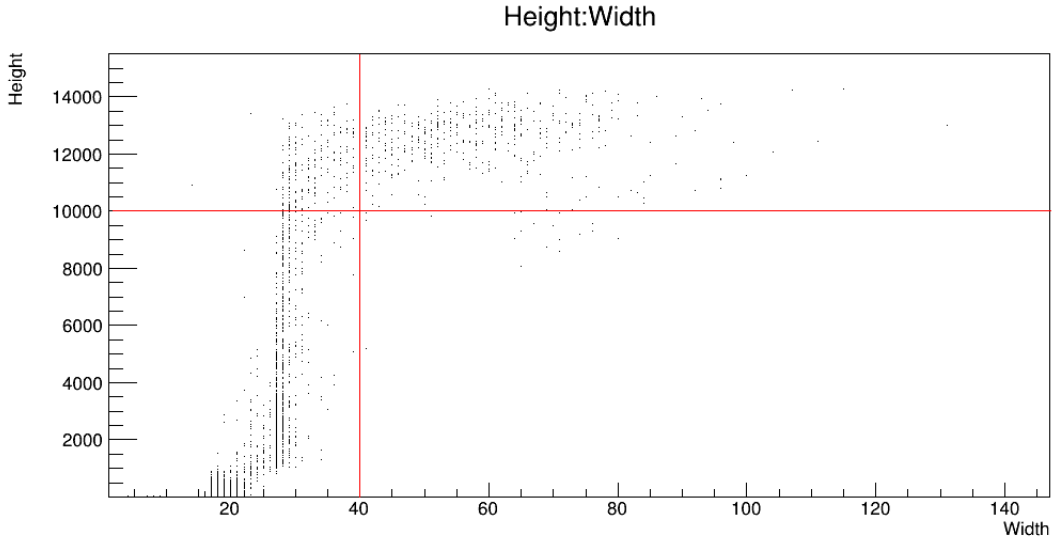

Figure 48: Plot showing the cuts made on the width and height of the signals recorded using detector-2 (right) at 35° separation angle.

4.2.3 Data Collection and Analysis

Once the ideal supply voltage and the discriminator threshold conditions were established, double coincidence event rates were recorded for the detector pair. The coincidence rate depends on the separation angle (shown in figure 49) between the two detectors. Events were recorded at separation angle from 0° to 35° at an interval of 5° and the event rate was calculated. The position of the detectors for different separation angles were calculated using the relation :

$$\mathrm{h} = \tan(\theta_{\mathrm{sep}})\mathrm{t} \tag{25}$$

where t is the horizontal distance between the two detectors, h is the vertical distance and θ_{sep} is the separation angle. The position of placement of the detectors and the height difference between the two detectors corresponding to each separation angle was cross checked using the technical drawings of the detectors.

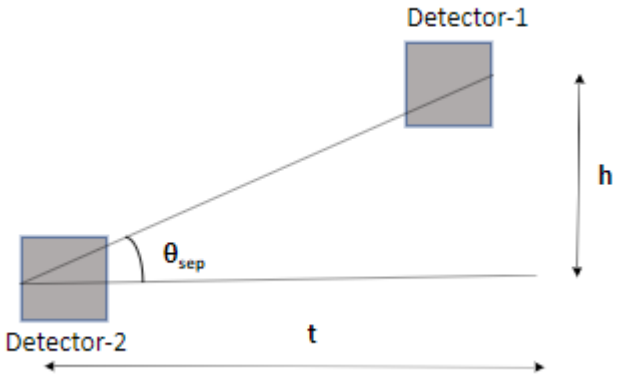

Figure 49: Sketch to show the separation angle between the two detectors, θ_{sep} which can be defined as h = tan(θ_{sep})t where h is the vertical height difference between the two detectors and t is the horizontal distance between the two detectors.

The muon flux formula was used to get a relation between the double coincidence event rate and the separation angle. For each value of separation angle, muon flux is given by:

$$\frac{\text{dN}}{\text{dAdtd}\Omega} = \text{I}_0\cos^2(\theta) \tag{26}$$

where θ is the zenith angle. The relation between the separation angle and zenith angle is shown in figure 50. I_0 is the muon flux at $\theta = 0°(0.007\ \text{cm}^2\text{s}^2\text{sr}^{-1})$ and the expressions for $\theta_{\text{max}}, \theta_{\text{min}}$ are,

$$\theta_{\text{min}} = \pi/2 + \arctan(\text{h} + \text{b/t}) \tag{27}$$

$$\theta_{\text{min}} = \pi/2 + \arctan(\text{h} - \text{b/t}) \tag{28}$$

In the above expressions, b is the thickness of the muon detectors,and as mentioned earlier, h is the vertical distance which is given by, equation 25. Using all the above equations the relation between separation angle and muon flux was deduced. Muon flux was calculated for each separation angle from 1° to 65° and the result is shown in figure 51.

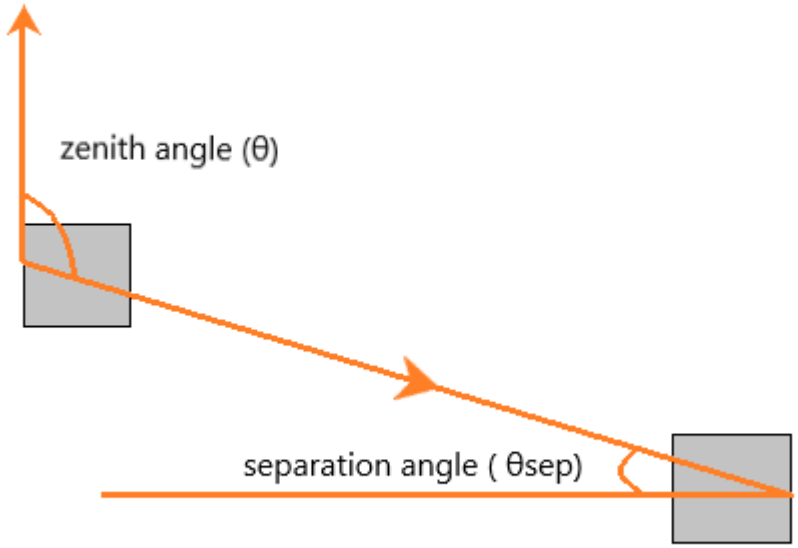

Figure 50: Sketch to show the relation between separation angle θ_{sep} and zenith angle θ.

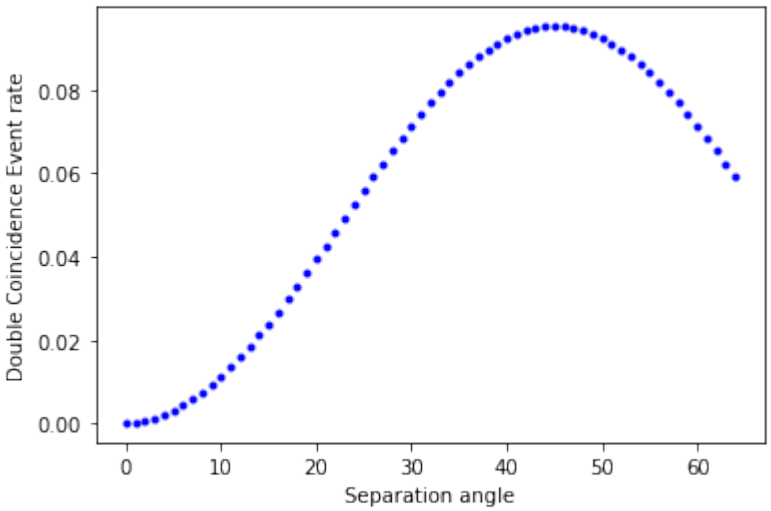

Figure 51: Expected double coincidence event rate(s^{-1}) calculated using muon flux formula as a function of separation angle (^{0}) between the two detectors.

A peak can be seen at 45° indicating maximum number of events at that angle, as muon flux is directly proportional to event rate. We see a peak in the curve because the integrated flux has a solid angle term along with the zenith angle terms and the

variation of solid angle with separation angle differs from the variation of zenith angle with separation angle.

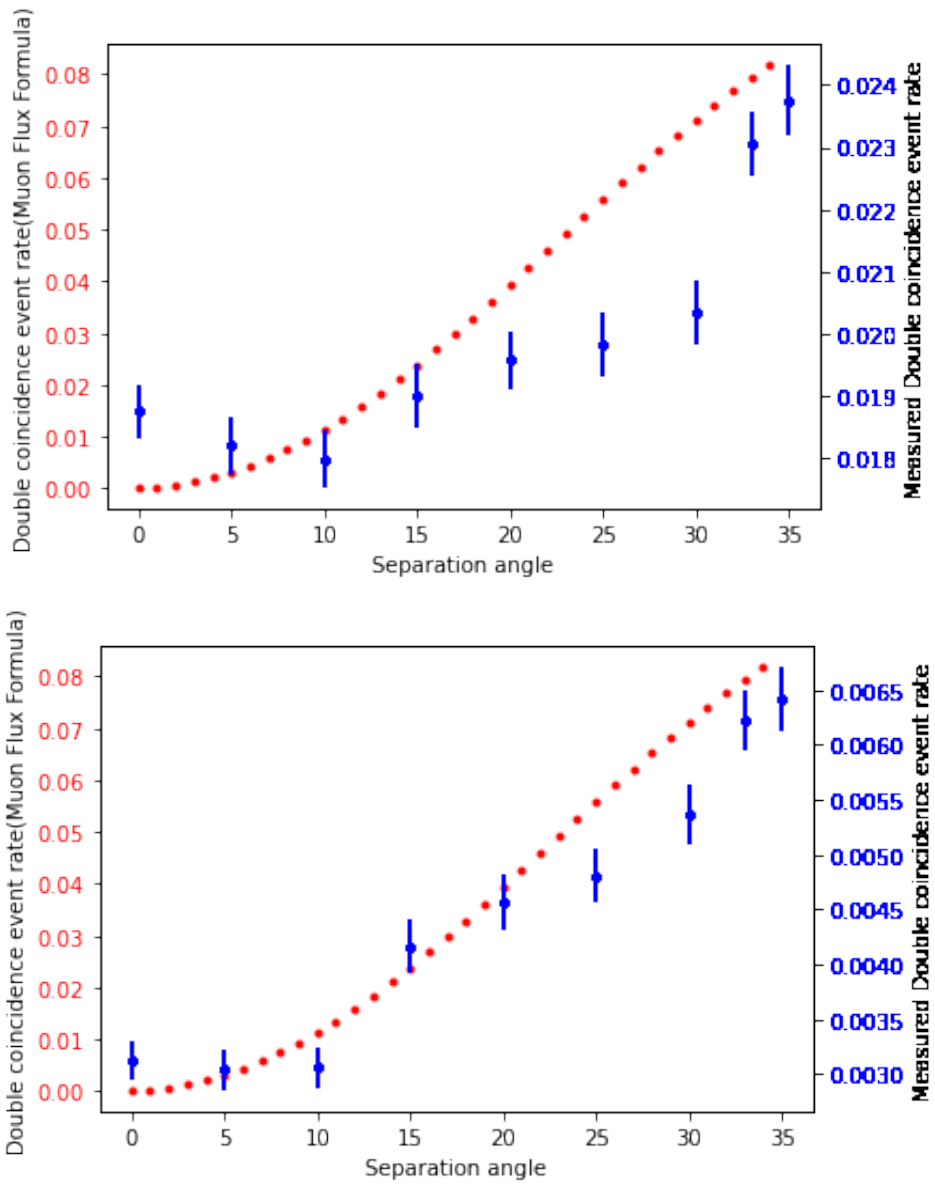

Figure 52: Comparison of the expected double coincidence event rate calculated using the muon flux formula and the experimental event rate before the height and width cut (left) and after the height and width cut (right).

The data obtained from both the detectors from this measurement is analysed using a processor. The histogram for the area of the signal, obtained from the processor is shown in figure 53. Since the energy deposited by muons is high compared to the gamma ray background, muon pulses have a larger area. To further make sure that

the events recorded by the detectors are muon events and not gamma ray double coincidence events, a height and a width cut was made as explained in section 4.2.2.

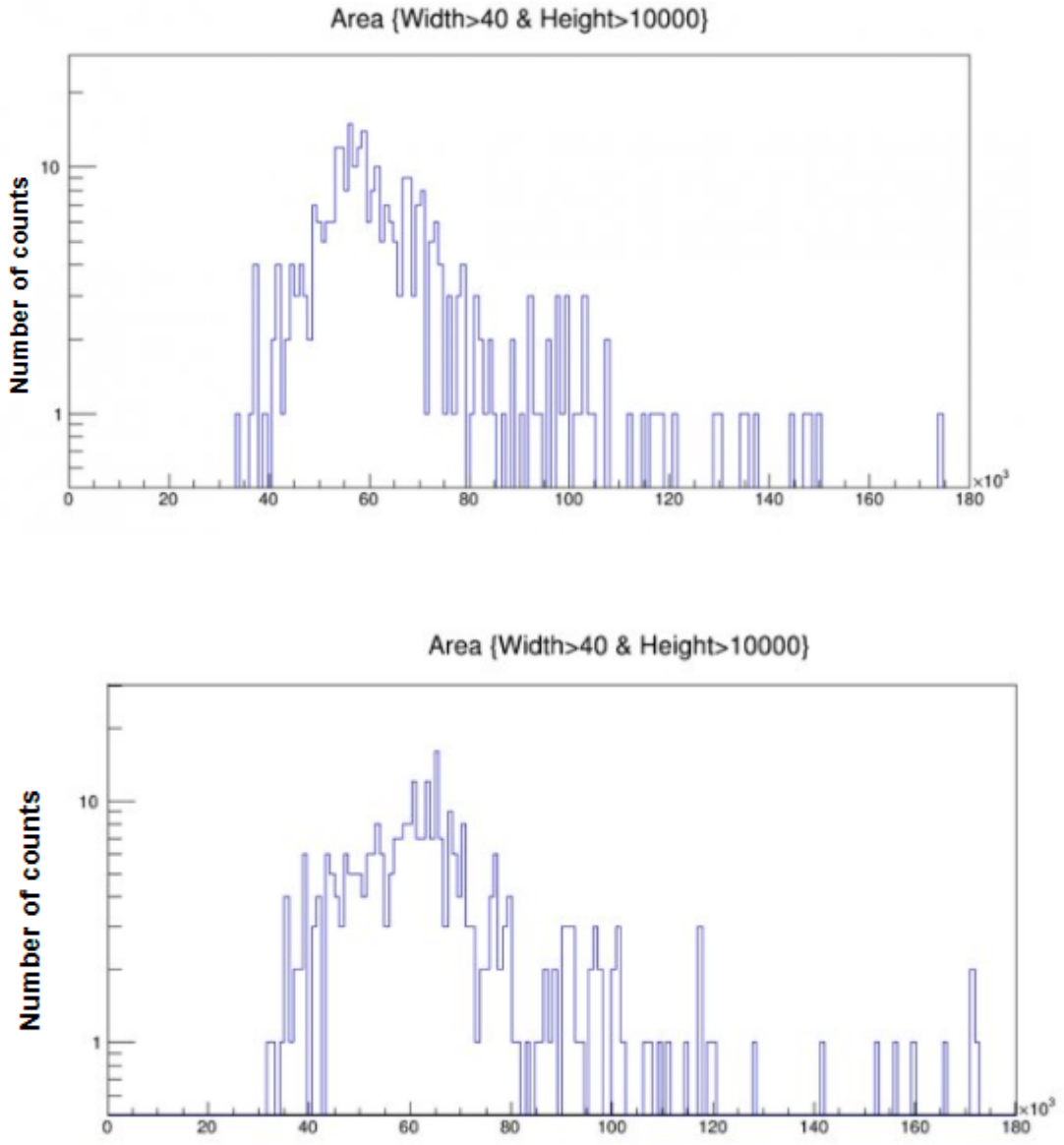

Figure 53: Area of the signal produced by the double coincidence muon events when the detectors are placed at a separation angle of 0° recorded in detector-1 (top) and detector-2 (bottom).

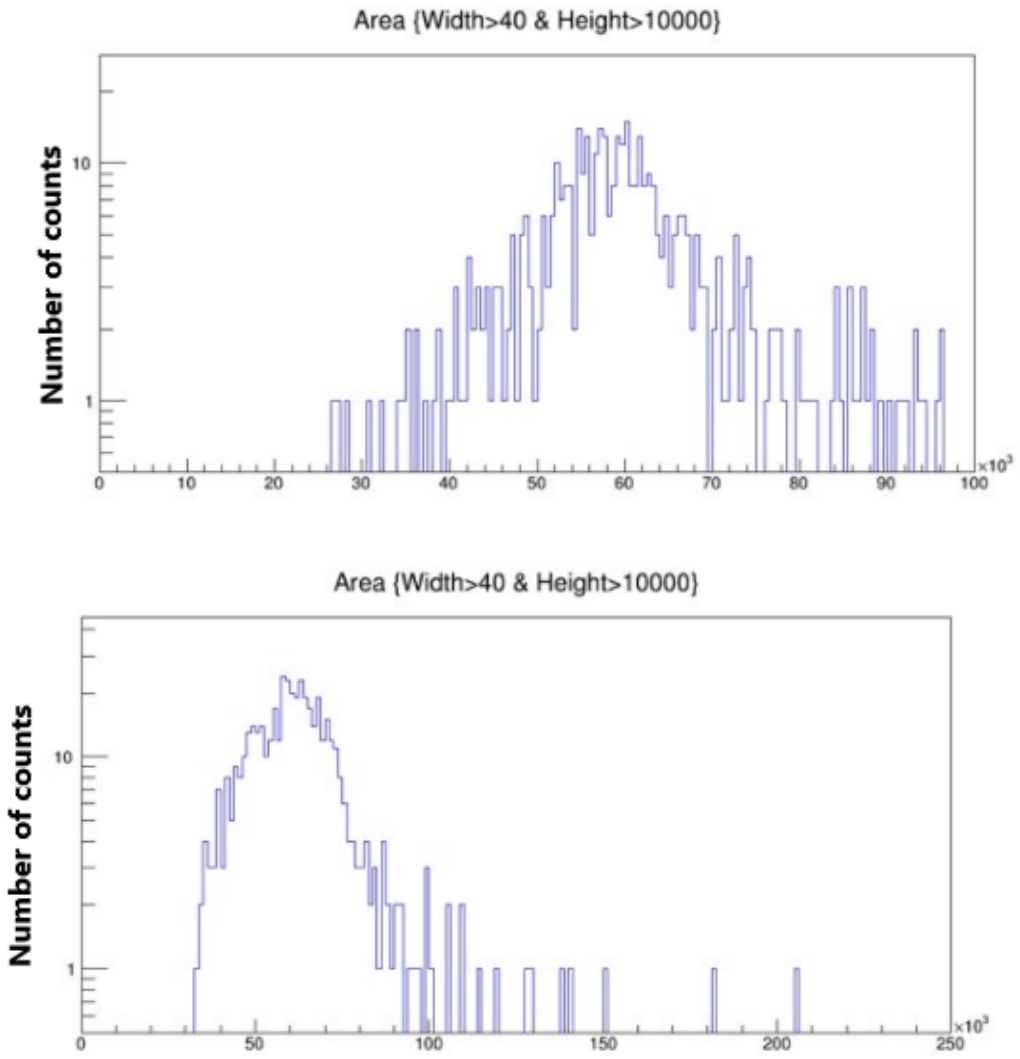

Figure 54: Area of the signal produced by the double coincidence muon events when the detectors are placed at a separation angle of 35° recorded in detector-1 (top) and detector-2 (bottom).

As it can be seen from the figure 52, the event rates recorded using the muon detectors are lower than the expected coincidence event rate calculated using the muon flux formula. The coincidence event rate (s^{-1})calculated using the muon flux formula uses the value of integral intensity of vertical muons (muons with zenith angle 0 °) which takes into account muons of all energies above 1 GeV [**?**]. One of the reasons for the difference in the measured and theoretical event rates can be the inefficiency of BC-412 scintillator material detectors to detect muons of very high energy range.

5 Calibration of Xenoscope using cosmic muons

As mentioned before, the motivation behind this project was to use a set of muon detectors for calibration purposes of Xenoscope. This will mainly evaluate the lifetime of the electrons using muons as a trigger and additionally check the homogeneity of the electric field inside the purity monitor. The initiation of the calibration process has been done in the course of this thesis and is explained in this chapter.

5.1 Muon Interaction in LXe

To get an estimate of the energy deposited by muons in LXe, the Bethe Bloch formula was used and its relation with the muon momentum is shown in figure 55.

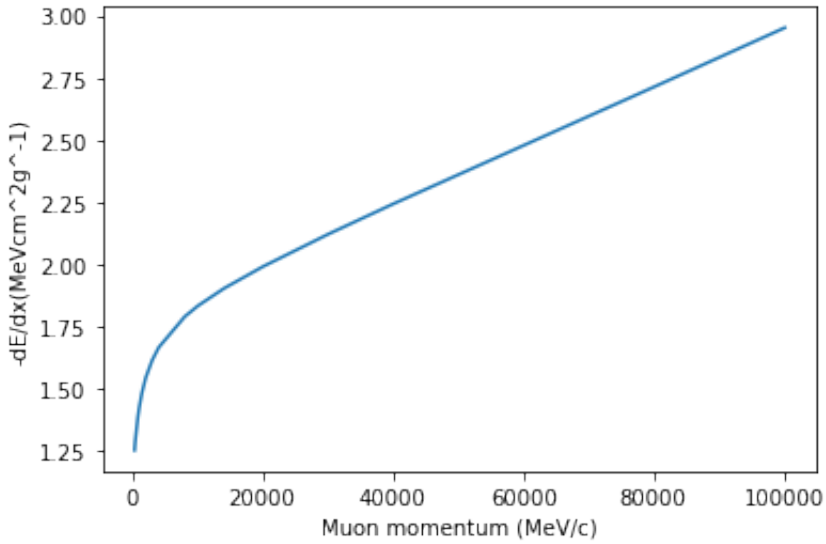

Figure 55: The stopping power of muons in LXe as a function of muon momentum calculated using the Bethe Bloch formula. The stopping power of 3 GeV muons in LXe, as seen in the plot, comes out to be 1.617 $\mathrm{MeVcm^2/g}$.

In our experiment, to have an estimate of the number of electrons produced by the energy deposited by muons in LXe, Bethe Bloch formula was used.

$(Z/A)_{Xe}$	0.411
ρ_{LXe}	2.85 g/cm^3
ρ_{GXe}	0.0001424 g/cm^3

To calculate the energy deposited by one 3 GeV muon in LXe and GXe,

$$\frac{dE}{dx}_{LXe} = 1.617\,\text{MeVcm}^2/\text{g}$$
$$\frac{dE}{dx}_{GXe} = 1.698\,\text{MeVcm}^2/\text{g}$$
$$\frac{dE}{dl}_{LXe} = 4.576\,\text{MeV/cm}$$
$$\frac{dE}{dl}_{GXe} = 2.417 \times 10^{-4}\,\text{MeV/cm}$$

The minimum distance travelled by the muon through LXe, inside the Purity Monitor is 15 cm.

$dE_{LXe} = 4.576 \times 15\,\text{MeV} = 68.64\,\text{MeV}$ where dE is the energy deposited by 3 GeV muons in LXe. The average ionization energy of LXe is 11.5 eV [35]. So the number of electrons produced by a muon of energy 3 GeV in LXe is approximately,

$$N(0)_{e,LXe} = (68.64/11.4) \times 10^6 = 6.021 \times 10^6 \tag{29}$$

$dE_{GXe} = 0.0002417 \times 15\,\text{MeV} = 0.00362\,\text{MeV}$ where dE is the energy deposited by 3 GeV muons in GXe. The average ionization energy of GXe is 12.1298 [36]. The number of electrons produced by a muon of energy 3 GeV in GXe comes out to be,

$$N(0)_{e,GXe} = (0.00384/12.1298) \times 10^6 = 3.168 \times 10^2 \tag{30}$$

These values of $N_e(0)$ were used to calculate the total number of electrons reaching the anode ($N_e(t)$), which was then plotted against the distance between the point of muon interaction and anode (Z). The number of electrons that will reach the anode depends on the survival probability of the electron (electron lifetime, τ). Equation 7 is used to deduce the relation shown in figures 56 and 57 .

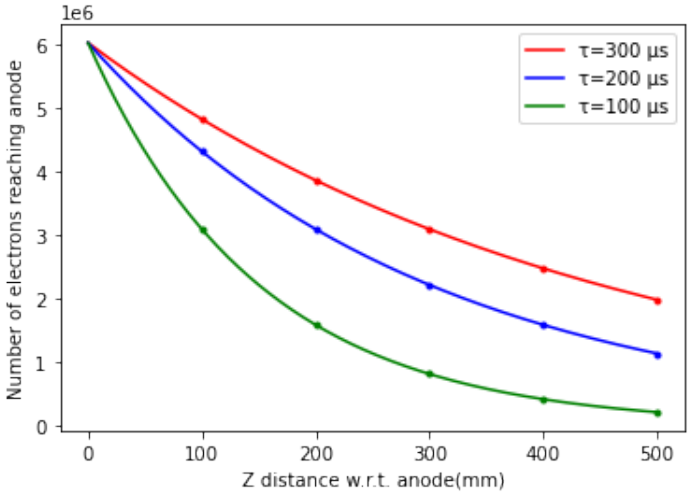

Figure 56: Relation between the total number of electrons reaching the anode and the Z-distance between the interaction point of muon and the anode in LXe for different values of electron lifetime.

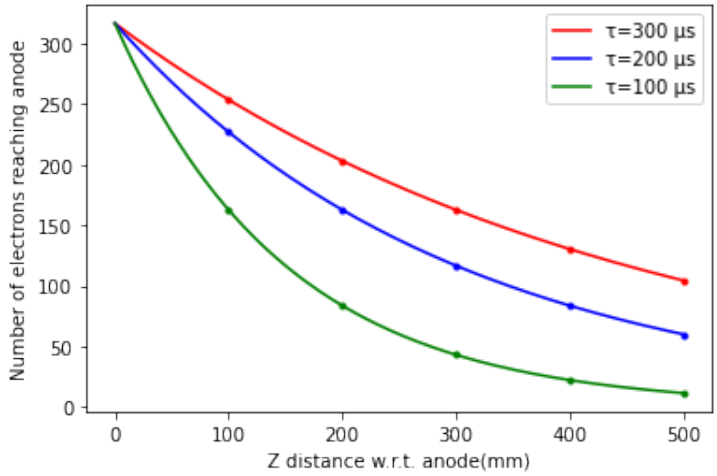

Figure 57: Relation between the total number of electrons reaching the anode and the Z-distance between the interaction point of muon and the anode in GXe for different values of electron lifetime.

5.2 Detector position optimization

The position of the detectors with respect to each other, was optimized to get maximum number of events. The relative position was parameterized by the separation angle between the two detectors, where a 0° separation angle means the two detectors are

parallel to each other. Figure 58 shows the muon detectors placed at two different separation angle.

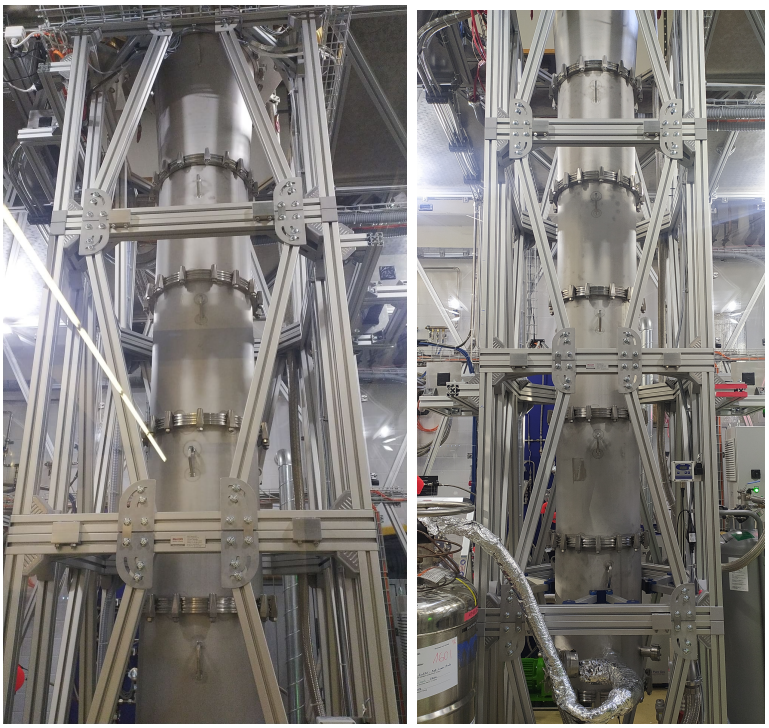

Figure 58: Two muon detectors placed around the demonstrator in the Xenoscope facility at the University of Zurich. The separation angle between the two detectors is 33°(left) and 0 °(right).

The muon flux formula was used to get a relation between the double coincidence event rate and the separation angle. As already mentioned in the previous chapter, section 4.2.3, for each value of separation angle, muon flux is be given by:

$$\frac{\mathrm{dN}}{\mathrm{dAdtd}\Omega} = \mathrm{I_0}\cos^2\theta \tag{31}$$

where θ is the zenith angle. A muon at zenith angle 0° travels perpendicular to the Earth's surface. Using the above equation, the relation between separation angle and muon flux was deduced. The flux formula is integrated from θ_{min} to θ_{max}, because only the muons travelling at a zenith angle between these angles will make a hit in both the muon detectors.

$$\frac{\mathrm{dN}}{\mathrm{dtdAd}\Omega} = \mathrm{I_0}\int_{\theta_{\mathrm{min}}}^{\theta_{\mathrm{max}}} \cos^2(\theta)\mathrm{d}\theta \tag{32}$$

where θ_{max} and θ_{min} are given by equation 27. The muon flux was calculated for each

separation angle from 1° to 65°, as shown in figure 59.

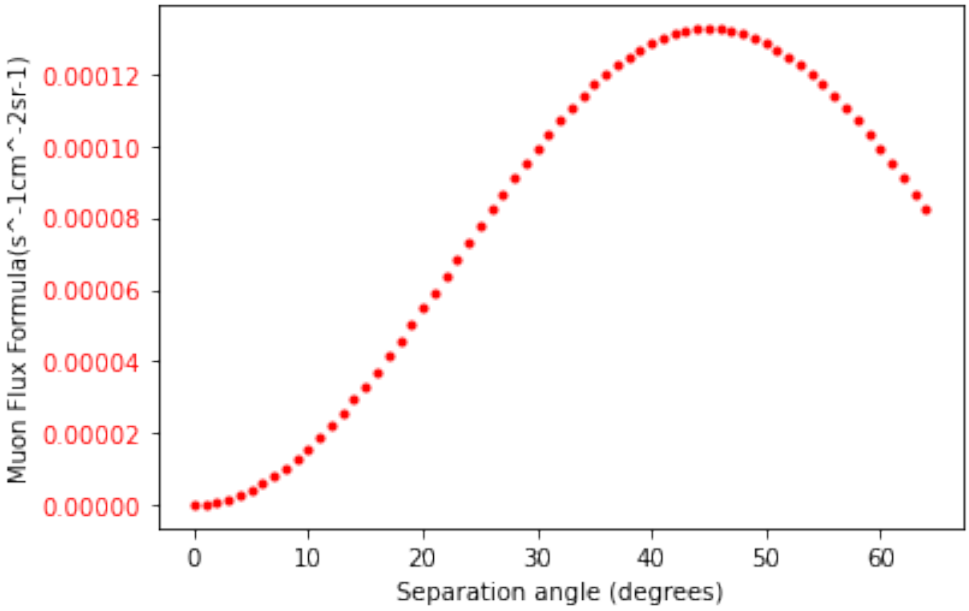

Figure 59: Muon flux calculated using the muon flux formula by taking the dimension of the detectors in use and the distance between them during the experiment into consideration as a function of the separation angle between the detectors.

The muon events that would make a hit in both the muon detectors are taken into account in this calculation. In our experiment, along with the double coincidence we would need the events to deposit energy in the LXe. So, to ensure that the double coincidence events also create a hit in the LXe, we used GEANT4 simulation.

GEANT4 is a C++ based Monte Carlo (MC) code originally developed at CERN. This package can be used for geometry construction, simulating the passage of particles through matter, incorporating physics models and recording hits [37]. For the purpose of simulation of events in Xenoscope, the GEANT4 simulation toolkit is used. A code was developed where the geometry of the cryostat and the TPC were added and the type of materials used in the detector were specified. The type and the properties of the particles that are to be simulated can be modelled using the PhysicsLists distributed with GEANT4. The output data of the simulation is stored in the ROOT file. The different variables of our interest were, the energy deposited in LXe, momentum of the particle or x,y,z direction.

A code is custom made for the simulation purposes of Xenoscope [38] which was used as a base code for this analysis. The muon panels with the dimensions same

as the ones we are using were added to it. A coincidence was defined when an event would deposit energy in both the muon panels and the sensitive volume, the TPC in our case. The separation angle between the detectors was changed by moving one of the detectors in the Z-direction and placing it at different position corresponding to different separation angles. A muon gun was placed near the stationary detector and muons with an energy of 4 GeV were released at these separation angles. The angle at which the muon gun would release the muons was also changed with the separation angle, to ensure the muon events making hits in both the muon panels. The simulation was run at an interval of separation angle 5° from 0° to 60° and the number of coincidences were noted. The relation between the number of coincidences(two muon panels and LXe) and separation angle is shown in figure 60.

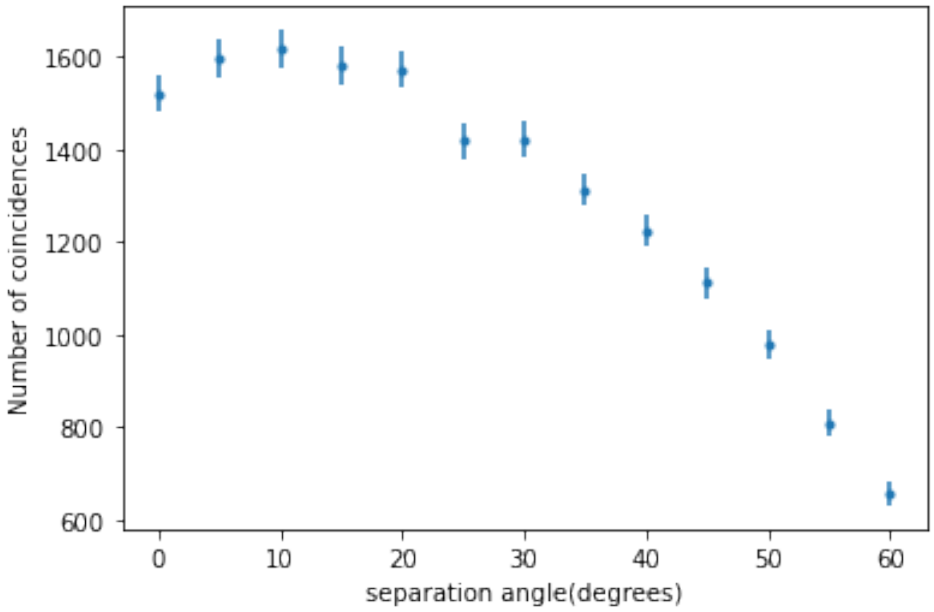

Figure 60: Relation between the number of muon events that deposit energy in both the muon detectors and the LXe (events in triple coincidence) and the separation angle between the muon detectors. The plot shows an uncertainty of $\sqrt{n}$ where n is the number of coincidences.

To obtain the optimal angle of separation, both plots were taken into consideration. After plotting the curves on the same plot and normalizing them, the optimized separation angle was found to be 30°, which is the intersection point of the two curves as shown in figure 61.

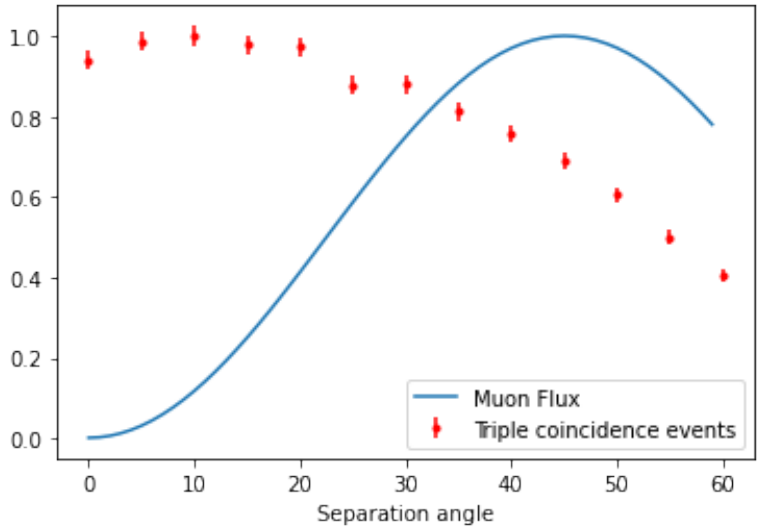

Figure 61: Muon flux and simulated triple coincidence events plotted against the separation angle. The separation angle at the intersection of these two plots is the optimal separation angle.

With increasing separation angle between the two muon detectors, the angle of incidence of the muons increases, making the path traversed by the muons inside the purity monitor steeper and thus increasing the the difference in time for the electrons produced by the muons to reach the anode. So, for large separation angles, the time window to record all the electrons in the purity monitor will be large.

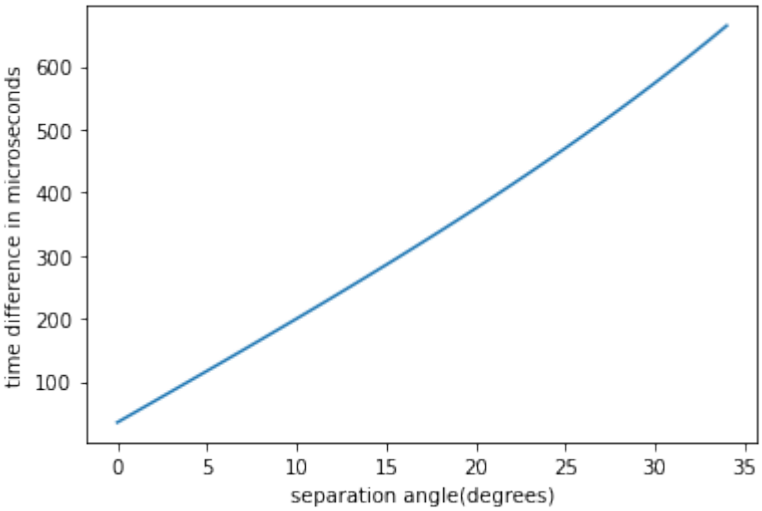

Figure 62: The time difference for electrons produced by one muon to reach the anode plotted against the separation angle between the two muon detectors.

Figure 62 shows the relation between the separation angle and the time difference, $\triangle t$. To obtain a better resolution on the Z-dependent measurement, the separation angle should be lower, zero degree being optimal, but because of the dimension of the detectors, the events corresponding to zero degree separation angle will include some muons traversing at an angle along with horizontally traversing muons, as shown in figure 63. The difference in time for electrons reaching anode at separation angle zero degree is 35.33 μs.

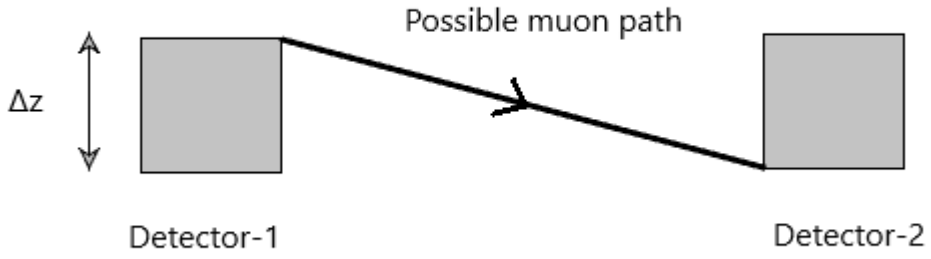

Figure 63: Schematic of the detectors at 0° separation angle. Despite the detectors being placed parallel to each other, the muons can travel at a small incidence angle because of the dimension of the detectors. This results in a time difference for the electrons produced by the same muon event to reach the anode.

$$\mathrm{v_{drift}} = \frac{\triangle \mathrm{z}}{\triangle \mathrm{t}} \tag{33}$$

The drift velocity of the electrons ($\mathrm{v_{drift}}$) inside the purity monitor is $\sim$ 1.5 mmμs. $\triangle$z is the height of the detector which is 5.3 cm. Using these values and equation 33, $\triangle$t comes out to be 35.33 μs.

Summary and Outlook

The DARWIN observatory, a proposed experiment that will be the ultimate dark matter detector using 50 tons of liquid xenon will be developed in the near future. A demonstrator for the DARWIN detector was built at the University of Zurich to contribute to the research and development of the DARWIN detector. One of the main challenges of Xenoscope is to prove the possibility of electrons drifting in LXe over a vertical length of 2.6 m. One of the ways to generate these electrons is to use cosmic ray muons, which can be detected and tagged using scintillator detectors. In the course of this work, a set of muon detectors were assembled and installed around Xenoscope. A double coincidence measurement was set up using these detectors where hits in both detectors registered within a coincidence time window acted as a trigger. For the experimental setup, NIM electronics were used, where the CAEN logic unit ensured the coincidence. The time window for coincidence was set to 40 ns which is optimal for registering muon events in both the detectors. A proper selection of threshold for the discriminator unit is set to exclude the electronic noise and low-energy gamma-ray events. The threshold was obtained with the help of radioactive sources: ^{60}Co and ^{137}Cs. To further make sure the events triggering the measurement are muon events, height and width cuts were made during analysis of the measured data. The muon event rate is a function of the separation angle between the two detectors. The relation between the measured double coincidence event rate and separation angle was then compared to the theoretical double coincidence event rate calculated using the muon flux formula given by equation 26. A GEANT4 simulation was used to obtain a first estimate of the event rates that will be observed in the two muon detectors and in LXe. This simulation along with the muon flux formula was also used to optimize the position of the muon detectors to get maximum event rates. The separation angle corresponding to the optimal detector position was found to be 30°. However, to have a better resolution in the z-direction, the separation angle should be set to 0° for the electron lifetime measurements in the future.

In the ongoing experiment with the first phase of Xenoscope, a purity monitor is

being used to measure the electron lifetime. Along with the xenon lamp trigger (which is used for the generation of electrons), the double coincidence muon events detected using the set up of muon detectors can be used to trigger the purity monitor. The set of muon detectors will be positioned at three different heights around the demonstrator. This corresponds to the muon events tagged by the two detectors having three different points of interaction in LXe and hence three different z position. This interaction results in ionisation and the initiation of the drifting of electron cloud taking place at three different heights in the purity monitor. Owing to the three different starting points, the drift time will be different for the three measurements. The total number of elections reaching the anode, $N_e(t)$ can be deduced from the charge collected by the anode of the purity monitor. $N_e(0)$ is the total number of electrons ionized by the muons at the interaction point. There is no way of experimentally measuring the value of $N_e(0)$ at different z-positions inside the purity monitor. A graphical method to calculate the electron lifetime can be used instead of a calculative approach because of this reason. Using the data sets from the three measurements, $N_e(t)$ can be plotted against the the drift time of the electrons. The drift time can be deduced from the waveform obtained by the purity monitor data. The data points from the three measurements can then be plotted and after an exponential fit, the value of electron lifetime (τ) can be calculated using

$$N_e(t) = N_e(0)e^{-t/\tau}. \tag{34}$$

Since the drift velocity of the electrons is dependent on the applied electric field, the muon detectors set up can also be used to check the homogeneity of the electric field inside the purity monitor. Non-homogeneous electric field can be indicated by a change in the drift velocity of the electrons. Therefore, for the drift velocity of the electrons to be constant, the applied electric field must be uniform. To check whether the drift velocity is constant, the relation between t_{drift} and the z coordinate can be used. Three measurements of t_{drift} can be plotted against their respective heights to determine the homogeneity of the applied electric field. In case of a linear fit of the plot, the drift velocity can be determined to be constant which will indicate the homogeneous nature of the electric field. The slope of the plot will give the value of the drift velocity.

In this way, the muon detectors set up can be used to ensure the two important conditions, purity measurement of LXe and homogeneity of the drift field, required to achieve the goal of Xenoscope.

Bibliography

[1] F. Zwicky, "On the masses of nebulae and of clusters of nebulae," *The Astrophysical Journal*, vol. 86, p. 217, 1937.

[2] J. Aalbers, F. Agostini, M. Alfonsi, F. Amaro, C. Amsler, E. Aprile, L. Arazi, F. Arneodo, P. Barrow, L. Baudis, and et al, "Darwin: towards the ultimate dark matter detector," *Journal of Cosmology and Astroparticle Physics*, vol. 2016, p. 017–017, Nov 2016.

[3] L. Baudis, Y. Biondi, M. Galloway, F. Girard, A. Manfredini, N. McFadden, R. Peres, P. Sanchez-Lucas, and K. Thieme, "Design and construction of xenoscope — a full-scale vertical demonstrator for the darwin observatory," *Journal of Instrumentation*, vol. 16, p. P08052, Aug 2021.

[4] L. Verde, P. Protopapas, and R. Jimenez, "Planck and the local universe: Quantifying the tension," *Physics of the Dark Universe*, vol. 2, no. 3, pp. 166–175, 2013.

[5] V. C. Rubin and J. Ford, W. Kent, "Rotation of the Andromeda Nebula from a Spectroscopic Survey of Emission Regions," , vol. 159, p. 379, Feb. 1970.

[6] A. Doroshkevich, V. Lukash, and E. Mikheeva, "A solution to the problems of cusps and rotation curves in dark matter halos in the cosmological standard model," *Physics-uspekhi - PHYS-USP*, vol. 55, 09 2012.

[7] H. Chandra, "Bullet cluster." `https://www.chandra.harvard.edu/graphics/resources/handouts/lithos/bullet_lithos.pdf`, 2006. [Online; accessed 10th March,2022].

[8] N. Aghanim, Y. Akrami, M. Ashdown, J. Aumont, C. Baccigalupi, M. Ballardini, A. J. Banday, R. B. Barreiro, N. Bartolo, and S. B. et al, "Planck 2018 results," *Astronomy and Astrophysics*, vol. 641, p. A6, sep 2020.

[9] R. Adam, P. A. R. Ade, N. Aghanim, Y. Akrami, M. I. R. Alves, F. Argüeso, M. Arnaud, F. Arroja, M. Ashdown, J. Aumont, and e. a. Baccigalupi, "Planck 2015 results," *Astronomy I& Astrophysics*, vol. 594, p. A1, Sep 2016.

[10] L. Roszkowski, "Particle dark matter: A theorist's perspective," *Pramana*, vol. 62, no. 2, pp. 389–401, 2004.

[11] J. Conrad, "Indirect Detection of WIMP Dark Matter: a compact review," in *Interplay between Particle and Astroparticle physics*, 11 2014.

[12] T. M. Undagoitia and L. Rauch, "Dark matter direct-detection experiments," *Journal of Physics G: Nuclear and Particle Physics*, vol. 43, p. 013001, Dec 2015.

[13] J. Silk *et al.*, *Particle Dark Matter: Observations, Models and Searches*. Cambridge: Cambridge Univ. Press, 2010.

[14] F. J. Kerr and D. Lynden-Bell, "Review of galactic constants," *Mon. Not. Roy. Astron. Soc.*, vol. 221, p. 1023, 1986.

[15] "Particle Data Group Dark Matter review 2021." `https://pdg.lbl.gov/2021/reviews/rpp2021-rev-dark-matter.pdf`. [Online; accessed 14th May, 2022].

[16] L. Baudis, A. Ferella, A. Kish, A. Manalaysay, T. M. Undagoitia, and M. Schumann, "Neutrino physics with multi-ton scale liquid xenon detectors," *Journal of Cosmology and Astroparticle Physics*, vol. 2014, pp. 044–044, jan 2014.

[17] J. Aalbers, F. Agostini, S. E. M. A. Maouloud, M. Alfonsi, L. Althueser, F. Amaro, J. Angevaare, V. C. Antochi, B. Antunovic, E. Aprile, and L. e. a. Arazi, "Solar neutrino detection sensitivity in darwin via electron scattering," 2020.

[18] F. Agostini, S. E. M. A. Maouloud, L. Althueser, F. Amaro, B. Antunovic, E. Aprile, L. Baudis, D. Baur, Y. Biondi, A. Bismark, P. A. Breur, and A. e. a. Brown, "Sensitivity of the darwin observatory to the neutrinoless double beta decay of ^{136}xe," 2020.

[19] E. Aprile and T. Doke, "Liquid xenon detectors for particle physics and astrophysics," *Rev. Mod. Phys.*, vol. 82, pp. 2053–2097, Jul 2010.

[20] P. Di Gangi, "The xenon road to direct detection of dark matter at lngs: The xenon project," *Universe*, vol. 7, no. 8, 2021.

[21] F. Agostini, S. E. M. Ahmed Maouloud, L. Althueser, F. Amaro, B. Antunović, E. Aprile, L. Baudis, D. Baur, Y. Biondi, A. Bismark, P. Breur, A. Brown, G. Bruno, R. Budnik, C. Capelli, J. Cardoso, D. Cichon, M. Clark, A. Colijn, and K. Zuber, "Sensitivity of the darwin observatory to the neutrinoless double beta decay of xe-136," *The European Physical Journal C*, vol. 80, 09 2020.

[22] L. Baudis, Y. Biondi, C. Capelli, M. Galloway, S. Kazama, A. Kish, P. Pakarha, F. Piastra, and J. Wulf, "A dual-phase xenon tpc for scintillation and ionisation yield measurements in liquid xenon," *The European Physical Journal C*, vol. 78, Apr 2018.

[23] E. Aprile and T. Doke, "Liquid xenon detectors for particle physics and astrophysics," *Reviews of Modern Physics*, vol. 82, p. 2053–2097, Jul 2010.

[24] L. Baudis, Y. Biondi, C. Capelli, M. Galloway, S. Kazama, A. Kish, P. Pakarha, F. Piastra, and J. Wulf, "A dual-phase xenon TPC for scintillation and ionisation yield measurements in liquid xenon," *The European Physical Journal C*, vol. 78, apr 2018.

[25] "Particle Data Group Dark Matter review 2021." `https://pdg.lbl.gov/2021/reviews/rpp2021-rev-cosmic-rays.pdf`. [Online; accessed 14th March, 2022].

[26] "Muon Stopping power and range tables." `https://pdg.lbl.gov/2021/AtomicNuclearProperties/adndt.pdf`. [Online; accessed 4th April,2022].

[27] "Organic Scintillators." `https://www.science.mcmaster.ca/radgrad/images/6R06CourseResources/4R6Notes4_ScintillationDetectors.pdf`. [Online; accessed 4th April,2022].

[28] S. Gobain, "Plastic scintillator material." `https://www.crystals.saint-gobain.com/radiation-detection-scintillators/plastic-scintillators/bc-400-bc-404-bc-408-bc-412-bc-416`, 2021. [Online; accessed 16th March,2021].

[29] SENSE, "Phtotmultiplier tube." `https://www.sense-pro.org/lll-sensors/pmt`. [Online; accessed 14th March,2022].

[30] D. Corning, "Electrical grease." `https://www.farnell.com/datasheets/319850.pdf`, 2021. [Online; accessed 16th March,2021].

[31] "Solid angle of a rectangular plate." https://vixra.org/pdf/2001.0603v2.pdf. [Online; accessed 8th April,2022].

[32] NIST, "Relation between interaction cross section and photon energy." https://www.nist.gov/pml/xcom-photon-cross-sections-database. [Online; accessed 18th March,2022].

[33] "CS-137/BA-137m isotope generator kit." https://www.spectrumtechniques.com/products/sources/isotope-generator-kit/, journal=Spectrum Techniques, 2021. [Online; accessed 14th March,2022].

[34] M.-R. Ioan, P. Cristian, V. Fugaru, S. Bercea, A. Celarel, and C. CENUSA, "Computational method for the determination of intense gamma-rays sources activity by using geant4," *Romanian Reports in Physics*, 12 2018.

[35] L. Baudis, P. Sanchez-Lucas, and K. Thieme, "A measurement of the mean electronic excitation energy of liquid xenon," *The European Physical Journal C*, vol. 81, Dec 2021.

[36] NIST, "Ionization energy of Gas xenon." https://webbook.nist.gov/cgi/cbook.cgi?ID=C7440633&Mask=28#Ion-Energetics. [Online; accessed 16th March,2021].

[37] S. Agostinelli, J. Allison, K. Amako, J. Apostolakis, H. Araujo, P. Arce, M. Asai, D. Axen, S. Banerjee, and G. Barrand, "Geant4—a simulation toolkit," *Nuclear Instruments and Methods in Physics Research Section A: Accelerators, Spectrometers, Detectors and Associated Equipment*, vol. 506, no. 3, pp. 250–303, 2003.

[38] "Demonstrator Xenonscope." https://github.com/Physik-Institut-UZH/DemonstratorXenonscope. [Online; accessed 4th April,2022].